crystals

MDPI

Article

Fabrication of Textured $0.685(Na_{0.5}Bi_{0.5})TiO_3$-$0.065BaTiO_3$-$0.25SrTiO_3$ Electrostrictive Ceramics by Templated Grain Growth Using $NaNbO_3$ Templates and Characterization of Their Electrical Properties

Kiran Andleeb [1], Doan Thanh Trung [1], John G. Fisher [1,*], Tran Thi Huyen Tran [1], Jong-Sook Lee [1,*], Woo-Jin Choi [2] and Wook Jo [2]

[1] Department of Materials Science and Engineering, Chonnam National University, 77 Yongbong-ro, Buk-gu, Gwangju 61186, Republic of Korea; kiran2k7@jnu.ac.kr (K.A.); 198881@jnu.ac.kr (D.T.T.); 188579@jnu.ac.kr (T.T.H.T.)

[2] School of Materials Science and Engineering, Ulsan National Institute of Science and Technology, Unist-gil 50, Eonyang-Eup, Ulju-gun, Ulsan 44919, Republic of Korea; cwj4134@unist.ac.kr (W.-J.C.); wookjo@unist.ac.kr (W.J.)

* Correspondence: johnfisher@jnu.ac.kr (J.G.F.); jongsook@jnu.ac.kr (J.-S.L.)

Abstract: Electrostrictive materials based on $(Na_{0.5}Bi_{0.5})TiO_3$ are promising lead-free candidates for high-precision actuation applications, yet their properties require further improvement. This study aims to enhance the electromechanical properties of a predominantly electrostrictive composition, $0.685(Na_{0.5}Bi_{0.5})TiO_3$-$0.065BaTiO_3$-$0.25SrTiO_3$, by using templated grain growth. Textured ceramics were prepared with 1~9 wt% $NaNbO_3$ templates. A high Lotgering factor of 95% was achieved with 3 wt% templates and sintering at 1200 °C for 12 h. Polarization and strain hysteresis loops confirmed the ergodic nature of the system at room temperature, with unipolar strain significantly improving from 0.09% for untextured ceramics to 0.23% post-texturing. A maximum normalized strain, S_{max}/E_{max} (d_{33}*), of 581 pm/V was achieved at an electric field of 4 kV/mm for textured ceramics. Textured ceramics also showed enhanced performance over untextured ceramics at lower electric fields. The electrostrictive coefficient Q_{33} increased from 0.017 m^4C^{-2} for untextured ceramics to 0.043 m^4C^{-2} for textured ceramics, accompanied by reduced strain hysteresis, making the textured $0.685(Na_{0.5}Bi_{0.5})TiO_3$-$0.065BaTiO_3$-$0.25SrTiO_3$ composition suitable for high-precision actuation applications. Dielectric properties measured between −193 °C and 550 °C distinguished the depolarization, Curie–Weiss and Burns temperatures, and activation energies for polar nanoregion transitions and dc conduction. Dispersive dielectric constants were found to observe the "two" law exhibiting a temperature dependence double the value of the Curie–Weiss constant, with shifts of about 10 °C per frequency decade where the non-dispersive THz limit was identified.

Keywords: $(Na_{0.5}Bi_{0.5})TiO_3$; electrostrictive materials; templated grain growth; relaxor; inverse piezoelectric properties; dielectric properties

Citation: Andleeb, K.; Trung, D.T.; Fisher, J.G.; Tran, T.T.H.; Lee, J.-S.; Choi, W.-J.; Jo, W. Fabrication of Textured $0.685(Na_{0.5}Bi_{0.5})TiO_3$-$0.065BaTiO_3$-$0.25SrTiO_3$ Electrostrictive Ceramics by Templated Grain Growth Using $NaNbO_3$ Templates and Characterization of Their Electrical Properties. *Crystals* **2024**, *14*, 861. https://doi.org/10.3390/cryst14100861

Academic Editor: Zhonghua Yao

Received: 11 September 2024
Revised: 26 September 2024
Accepted: 27 September 2024
Published: 30 September 2024

1. Introduction

Piezoelectric materials, capable of converting mechanical energy into electrical energy and vice versa, play a crucial role in various applications such as sensors, actuators, and energy storage devices [1,2]. Lead zirconate titanate (PZT) is particularly notable for its favorable properties, including a robust piezoelectric effect and high Curie temperature [3], making it widely applicable [4,5]. However, the environmental and health risks associated with the high lead content (up to 60 wt%) in PZT-based devices necessitate the exploration of lead-free alternatives or the enhancement of existing materials to compete with PZT.

Bi-based perovskites are attractive alternatives to PZT because Bi^{3+} exhibits a similar electronic configuration to Pb^{2+} [1]. Among them, $(Na_{0.5}Bi_{0.5})TiO_3$ (NBT) stands out

for its promising ferroelectric properties [1,6]. Pure NBT exhibits relaxor ferroelectric behavior with a rhombohedral (*R*3*c* space group) or possibly monoclinic structure (*Cc* space group) [7,8]. Phase transitions from rhombohedral to tetragonal (*P*4*bm*) and from tetragonal to cubic ($Pm\bar{3}m$) occur at approximately 255 °C and 540 °C, respectively [7]. Although NBT has a large remanent polarization of 38 $\mu C/cm^2$, its large coercive field of 73 kV/cm and high conductivity complicate the polling process [1,9]. Several solid solutions of NBT have been developed to address these limitations [1,6,10]. Initially, the depolarization temperature of NBT around 200 °C was thought to be a limiting factor, as ferroelectric order is disrupted at this temperature [1,11,12]. However, later studies found significant strains around this temperature due to a reversible electric field-induced relaxor to ferroelectric phase transition, also known as incipient ferroelectricity [4,13,14]. Giant strains have been recorded in such systems, but a large strain hysteresis is also present [4,11,13–17].

Electrostriction, a property present in all dielectric materials [18], is particularly large in relaxor ferroelectrics, especially at the boundary between non-ergodic and ergodic phases (sometimes referred to in the literature as ferroelectric and antiferroelectric phases) [19–21]. However, at this boundary, strain hysteresis is still high. Strain hysteresis can be further reduced when the ergodic phase dominates [21,22]. This results in hysteresis-free electrostrain generated from a nearly pure electrostrictive effect, which is attractive for high-precision positioning devices [21–23]. Although the electrostrictive effect is relatively small compared to both electric field-induced phase transitions and the inverse piezoelectric effect that yield higher strains, electrostriction offers several advantages. These include the absence of remanent strain, which provides fatigue resistance, and temperature stability, allowing for usage over a wide temperature range. Additionally, electrostriction does not require poling and exhibits low hysteresis, resulting in precise displacement accuracy [22,23]. NBT-based systems are particularly attractive as the electrostrictive effect can be easily achieved through simple compositional modifications [19,21,22,24]. Therefore, enhancing electrostrictive strain in NBT-based systems can be highly beneficial for high-precision positioning in actuators. Although they are now receiving more attention, the amount of work on electrostrictive NBT compositions is limited compared to ferroelectric and incipient ferroelectric NBT-based materials.

Among NBT-based solid solutions, $(Na_{0.5}Bi_{0.5})TiO_3$-$BaTiO_3$ (NBT-BT) is extensively studied [25–29]. However, at the MPB, the depolarization temperature (T_d), where large strains are observed due to electric field-induced phase transitions, is higher than room temperature [1,6,30]. The depolarization temperature can be depressed to room temperature by adding a third component such as $(K_{0.5}Na_{0.5})NbO_3$ or $SrTiO_3$ [31–33]. The ternary electrostrictive composition 0.685$(Na_{0.5}Bi_{0.5})TiO_3$-0.065 $BaTiO_3$-0.25 $SrTiO_3$ (0.685NBT-0.065BT-0.25ST) is selected for the present study. Wang et al. showed that the ergodic state dominates at room temperature for this composition, due to a decrease in depolarization temperature to below room temperature by the introduction of $SrTiO_3$ (ST) [31,32]. At the same time, the value of the direct piezoelectric charge constant d_{33} decreases considerably, and the strain is mostly caused by electrostriction [32]. Therefore, the electrostrictive effect is predominant in this specific composition. As mentioned above, the electric field-induced strains in electrostrictive compositions are lower than those of conventional or incipient ferroelectric materials. The objective of the present study is to further enhance the electrostrain in this composition to simultaneously realize both low hysteresis and large electrostrictive effects.

Microstructure engineering offers a pathway to enhance the properties of polycrystalline ceramics to match those of single crystals. Although single crystals always show superior properties compared to their polycrystalline counterparts due to their strong anisotropy [18,34], they are more expensive to prepare than polycrystalline ceramics and usually take a long time to grow. Texturing is a promising method for achieving the desired microstructure and properties in polycrystalline ceramics [35–37]. Textured ceramics show improved properties by aligning the grains in a particular orientation. This is achieved via the preparation of anisotropic templates with specific crystallographic properties, such as plate-like template particles. These templates are mixed with matrix powder, binder,

and other organic additives to form a slurry, which is then tape-cast. The alignment of template particles in the cast tape, facilitated by the shear force of the doctor blade, is crucial for the subsequent grain orientation process [38]. After casting, the tapes are cut, stacked, pressed, and sintered. During sintering, matrix grains grow on the template particles, aligning themselves in the same crystallographic direction. Typically, template particles are micron-sized with a high aspect ratio, surpassing the size of matrix powder particles. The contrast in surface energy between matrix and template particles generates a driving force for the template grain growth process. The fabrication of NBT-based textured ceramics usually follows the templated grain growth (TGG) process [39,40]. TGG involves calcining raw materials to produce matrix powder, which is then mixed with template particles, tape-cast, and sintered. $NaNbO_3$ templates (NN templates) are commonly used in TGG of NBT-based systems [35,36]. A high degree of texture of >90% and high strain has been previously achieved in NN template textured NBT-based systems [41], showing that $NaNbO_3$ templates are effective for the fabrication of textured ceramics.

Limited studies have been carried out on the texturing of electrostrictive NBT-based compositions. In the case of $0.97[Bi_{1/2}(Na_{0.78}K_{0.22})_{1/2}]TiO_3$-$0.03BiAlO_3$, the room temperature electrostrictive coefficient for textured ceramics increases to 0.043 $m^4C^{-2,}$ which is two times greater than in the untextured samples [42]. In the present study, we aim to enhance the electrostrictive properties of 0.685NBT-0.065BT-0.25ST ceramics [32] with high strain and reduced strain hysteresis by the fabrication of textured ceramics to improve their performance and applicability in high-precision actuation devices. We use plate-like $NaNbO_3$ templates with a perovskite structure, synthesized by molten-salt synthesis, to produce textured 0.685NBT-0.065BT-0.25ST ceramics.

2. Materials and Methods

2.1. Powder Preparation

Powder of the composition $0.685(Na_{0.5}Bi_{0.5})TiO_3$-$0.065BaTiO_3$-$0.25SrTiO_3$ (0.685NBT-0.065BT-0.25ST) is prepared by using the mixed oxide process. Stoichiometric amounts of raw materials Na_2CO_3 (Acros Organics, Geel, Belgium, 99.5%), Bi_2O_3 (Alfa Aesar, Ward Hill, MA, USA, 99.9%), $SrCO_3$ (Aldrich, St. Louis, MO, USA, 99.9%), $BaCO_3$ (Alfa Aesar, 99.8%) and TiO_2 (Alfa Aesar, 99.8%) are dried at 250 °C for 5 h to remove any moisture, weighed, and ball milled in a planetary ball mill at 500 rpm for a total milling time of 3 h in high purity ethanol (99.9%) with a ZrO_2 liner and milling media. The mill was operated for thirty-six 5 min cycles, with a 1 min pause between each cycle to allow the slurry to cool. After milling, most of the ethanol is evaporated from the slurry using a hotplate/magnetic stirrer. The remaining ethanol is evaporated by placing the slurry in an oven at 70 °C overnight. The dried mixture is ground in an agate mortar and pestle, sieved through a 180 µm sieving mesh, placed in a high-purity alumina crucible with a lid, and calcined at 850 °C for 3 h. The calcined powder is ball-milled for 24 h in a standard ball mill in high-purity ethanol (99.9%) with a polypropylene bottle and ZrO_2 milling media, followed by grinding and sieving to remove agglomerates.

2.2. $NaNbO_3$ Template Preparation

To prepare plate-shaped single crystalline $NaNbO_3$ templates (NN template), a double molten salt synthesis method is utilized [43,44]. Initially, stoichiometric amounts of Na_2CO_3 (Acros Organics, 99.5%), Bi_2O_3 (Alfa Aesar, 99.9%), and Nb_2O_5 (Daejung, Siheung, Republic of Korea, 99.9%) for the preparation of $Bi_{2.5}Na_{3.5}Nb_5O_{18}$ (BNN5) are dried at 250 °C for 5 h and ball-milled in a standard ball mill for 12 h in high-purity (99.9%) ethanol with ZrO_2 milling media. Subsequently, NaCl salt (Sigma-Aldrich, 99.5%) is added at a weight ratio of (oxides + carbonate) to salt of 1:1.5, and the mixture is further ball-milled for 12 h. Most of the ethanol is evaporated using a hotplate/magnetic stirrer. The remaining ethanol is evaporated by placing the slurry in an oven at 70 °C overnight. The dried mixture is then ground using an agate mortar and pestle and heat-treated in an alumina crucible with a

°C for 5 h and ball-milled in a standard ball mill for 12 h in high-purity (99.9%) ethanol with ZrO_2 milling media. Subsequently, NaCl salt (Sigma-Aldrich, 99.5%) is added at a weight ratio of (oxides + carbonate) to salt of 1:1.5, and the mixture is further ball-milled for 12 h. Most of the ethanol is evaporated using a hotplate/magnetic stirrer. The remaining ethanol is evaporated by placing the slurry in an oven at 70 °C overnight. The dried mixture is then ground using an agate mortar and pestle and heat-treated in an alumina crucible with a lid at 1125 °C for 4 h. The resulting product (BNN5 + NaCl) is soaked and washed in hot deionized water to remove the NaCl.

In the second step, BNN5 and a 100% mass excess of Na_2CO_3 (i.e., twice the amount of Na_2CO_3 required for stoichiometry) are mixed in high-purity ethanol (99.9%) using a magnetic stirrer for 2.5 h. NaCl is then added to the mixture, which is further mixed for 2.5 h at a (BNN5 + Na_2CO_3) to salt weight ratio of 1:1.5. After drying, the mixture undergoes heat treatment in an alumina crucible with a lid at 950 °C for 4 h to achieve the topochemical conversion of BNN5 to perovskite $NaNbO_3$ templates. The final product is soaked in water and then in 4 M HCl acid to remove excess Bi_2O_3, followed by alternate washes with 3 M HCl acid and water to eliminate NaCl and Bi_2O_3 byproducts.

2.3. Tape-Casting and Sintering

Details of the tape-casting process are given in Figure 1 [45]. For dispersion milling, a solution of methyl ethyl ketone (Daejung, 99.9%) and ethanol (Daejung, 99.9%) (MEK/ET) is used as a solvent with the weight ratio of MEK/ET of 66/34%. Triethanolamine (Sanchun, Seoul, Republic of Korea, 99%) is used as a dispersant. Ball milling was carried out using a standard alumina ball mill with ZrO_2 milling media. In the second step, polyvinyl butyral (PVB, Butvar B79, Eastman, Kingsport, TN, USA) is used as a binder, while benzyl n-butyl phthalate (Alfa Aesar, 98%) and Polyethylene glycol 400 (Daejung, GR grade) are used as the plasticizers. Between 0 and 9 wt% of $NaNbO_3$ templates are added. The weight percentages of the slurry components of the ceramic powder are provided in Table 1. For the textured ceramics, the total solid loading includes both the ceramic powder and the NN template content. Solid loading is 50% of the total slurry weight.

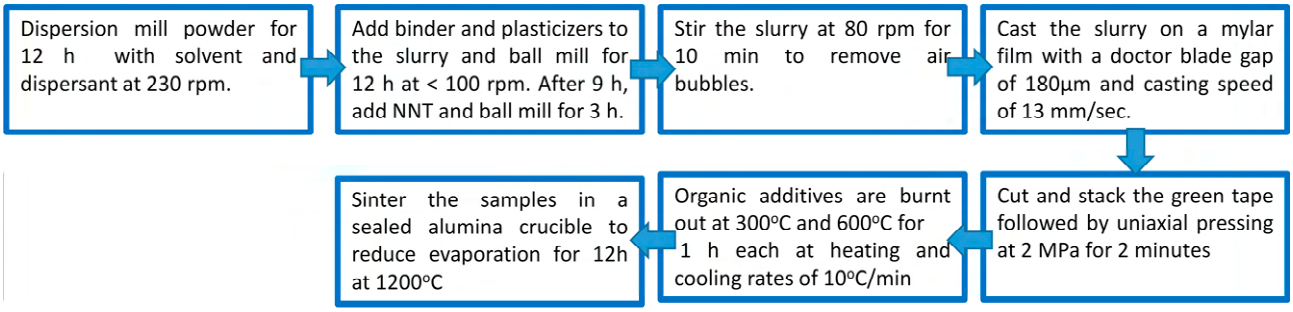

Figure 1. Experimental procedure of tape-casting and sample preparation.

Table 1. Weight percentages of slurry components.

Additive	Name	Weight %
Solvent	Methyl ethyl ketone + ethanol (66/34%)	40.405
Dispersant	Triethanolamine	1.06
Plasticizer	benzyl n-butyl phthalate	3.435
Plasticizer	Polyethylene glycol 400	0.93
Binder	Polyvinyl butyral	4.165
Solids	0.685NBT-0.065BT-0.25ST powder with 0~9 wt% NN templates	50

For sintering, samples are buried in packing powder of the same composition and sintered in a double alumina crucible with lids to reduce the evaporation of alkali metals. The inner crucible and lid are sealed with alumina cement (Ceramabond 503, Aremco, Valley Cottage, NY, USA). The cement was fired according to the manufacturer's instructions. Samples are sintered in air at 1200 °C for 5–20 h with heating and cooling rates of 5 °C/min.

2.4. Characterization

Phase purity and structure of the calcined powder and as-sintered bulk ceramics were examined using X-ray diffraction (XRD, X'Pert PRO, PANalytical, Almelo, The Netherlands)

in Bragg–Brentano geometry using CuKα radiation with a scan range of 20–80°2θ, a step size of 0.026° and a scan speed of 3°/min. The phase purity and morphology of the BNN5 precursor and NN templates are analyzed by XRD and scanning electron microscopy (SEM, S-4700, Hitachi, Tokyo, Japan). Samples for SEM are Pt-coated. The degree of texture of as-sintered bulk ceramics is calculated using the Lotgering factor formula [46]. For microstructure analysis, bulk ceramic samples are cross-sectioned using a low-speed diamond wheel saw, polished to a 1 µm finish using diamond paste, and thermally etched for 1 h at 1100 °C. Samples are Pt-coated and examined by SEM. Electron probe microanalysis (EPMA, JEOL JXA-8530F PLUS, Tokyo, Japan) was carried out on a cross-sectional surface of a textured sample that was sintered for 12 h. The sample is polished to a 1 µm finish using diamond paste but not thermally etched. Wavelength-dispersive spectroscopy (WDS) analysis was carried out using an accelerating voltage of 15 kV. $NaAlSi_2O_6$, $Bi_4Ge_3O_{12}$, $KNbO_3$, $BaTiO_3$ and $SrTiO_3$ were used as standards. The sample was carbon-coated.

To measure dielectric properties, the upper and lower surfaces of the samples are parallel polished with grade #2000 and #4000 SiC papers. Silver paste electrodes (16032 PELCO, Ted Pella, Redding, CA, USA) are applied on both surfaces. Samples are loaded in a heating/cooling stage (THMS600, Linkam, Tadworth, UK). Measurements are carried out from −193 °C to 50 °C in flowing N_2 to reduce humidity in the stage. Impedance is measured using an impedance analyzer (HP4284A, Agilent, Santa Clara, CA, USA) from 10^6 Hz to $10^{1.4}$ Hz (=25.1 Hz) for a total of 47 pts at a 0.1 interval in logarithmic frequencies with heating and cooling rates of 1 °C/min. To prepare samples for measurement of ferroelectric and inverse piezoelectric properties, the top and bottom surfaces of the samples are polished with grade #2000 SiC and #4000 SiC papers. Silver electrodes (DS-PF-7472, Daejoo, Siheung, Republic of Korea) are applied on the top and bottom surfaces. Polarization (P) and strain (S) hysteresis vs electric field is measured in a commercial apparatus, aixPES (aixACCT system GmbH, Aachen, Germany) at 1 Hz under electric fields up to 4 kV/mm. Each sample was measured three times, with three cycles in each measurement.

3. Results and Discussion

3.1. Powder Preparation

Figure 2 shows an XRD pattern of the calcined powder. The pattern can be indexed with JCPDS (Joint Committee on Powder Diffraction Standards) pattern No. 01-089-3109 for cubic (space group $Pm\bar{3}m$) $(Na_{0.5}Bi_{0.5})TiO_3$. No secondary phase peaks are visible.

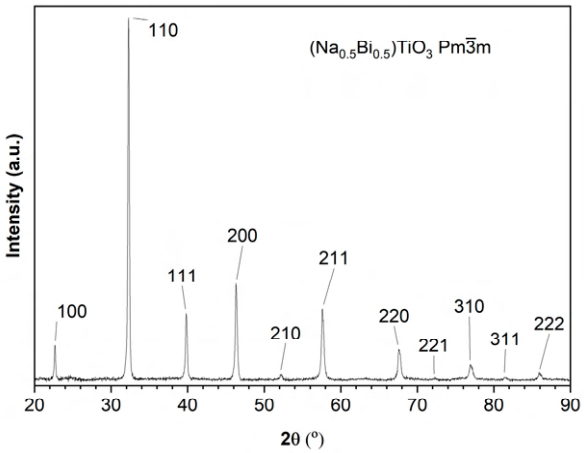

Figure 2. XRD pattern of calcined $0.685NBT$-$0.065BT$-$0.25ST$ powder.

3.2. $NaNbO_3$ Template Preparation

Figure 3a shows an SEM micrograph of the $Bi_{2.5}Na_{3.5}Nb_5O_{18}$ (BNN5) precursor templates. The templates have a plate-like morphology and are up to ~20 µm in diameter. Figure 3c shows the XRD pattern of the BNN5 precursor corresponding to JCPDS pattern No. 42-0399 for $Bi_{2.5}Na_{3.5}Nb_5O_{18}$. Peaks belonging to $Bi_{2.5}Na_{2.5}Nb_4O_{15}$ (BNN4), Na_3NbO_4, and an unknown phase are also identified. Figure 3b shows an SEM micrograph of the NN templates prepared using the BNN5 precursor. It can be observed that the NN templates retained the plate-like morphology of the precursor BNN5 templates. Moreover, a high aspect ratio of templates is achieved, which is necessary for mechanical alignment under shear force during tape casting [47]. The NN templates are not as uniform and

and an unknown phase are also identified. Figure 3b shows an SEM micrograph of the NN templates prepared using the BNN5 precursor. It can be observed that the NN templates retained the plate-like morphology of the precursor BNN5 templates. Moreover, a high aspect ratio of templates is achieved, which is necessary for mechanical alignment under shear force during tape-casting [47]. The NN templates are not as uniform and smooth as the BNN5 templates due to the topochemical reaction and washing steps. The following reactions occur during the two-step molten salt synthesis of NN templates [44]:

$$5\ Bi_2O_3 + 7\ Na_2CO_3 + 10\ Nb_2O_5 \rightarrow 4\ Bi_{2.5}\ Na_{3.5}\ Nb_5O_{18} + \uparrow 7\ CO_2 \quad (1)$$

$$4\ Bi_{2.5}Na_{3.5}Nb_5O_{18} + 3\ Na_2CO_3 \rightarrow 20\ NaNbO_3 + 5\ Bi_2O_3 + \uparrow 3\ CO_2 \quad (2)$$

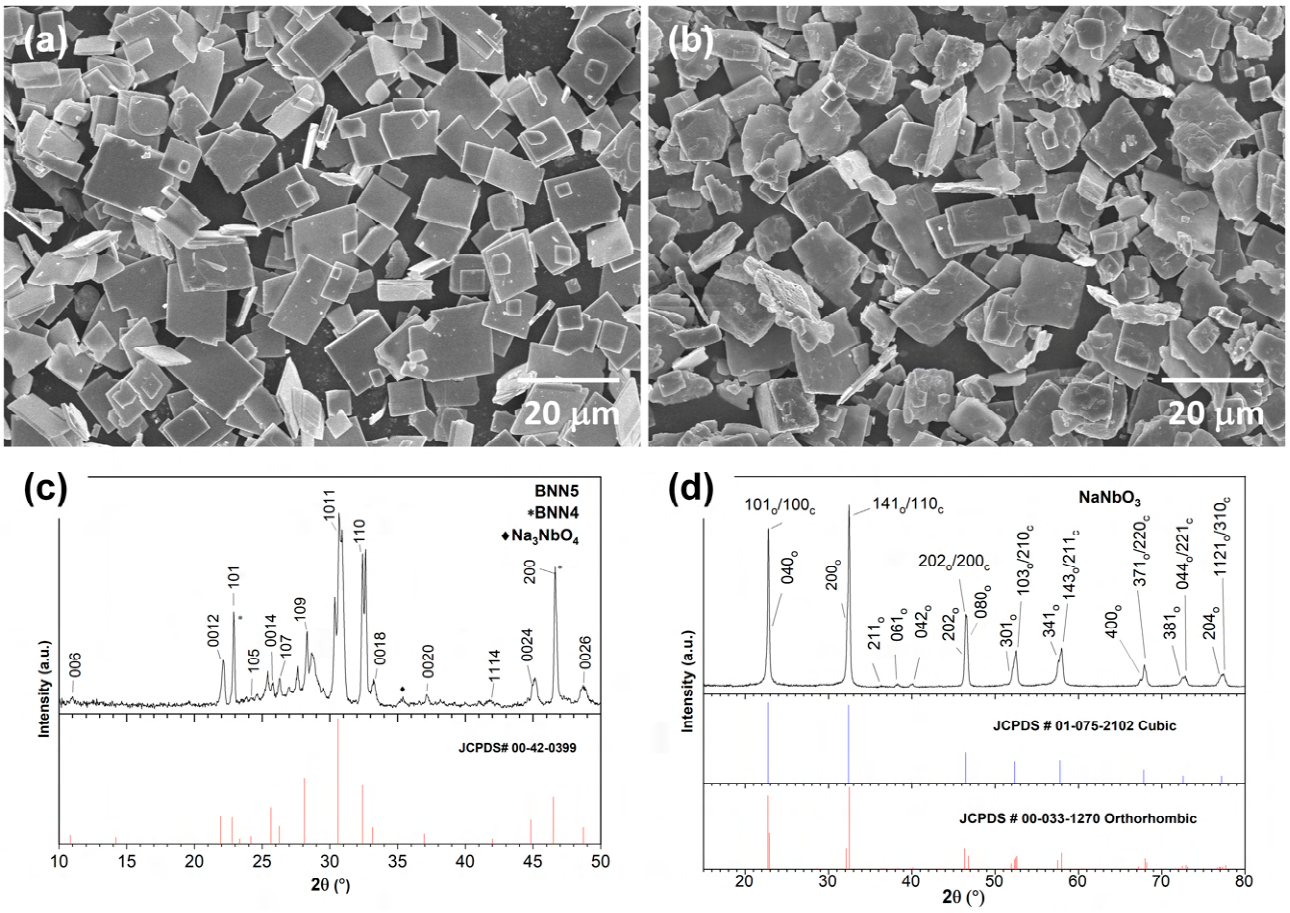

Figure 3. SEM micrographs of (**a**) $Bi_{2.5}Na_{3.5}Nb_5O_{18}$ precursor; (**b**) $NaNbO_3$ templates. XRD patterns of (**c**) $Bi_{2.5}Na_{3.5}Nb_5O_{18}$ precursor; (**d**) $NaNbO_3$ templates.

3.3. Texture Development

Figure 3d shows the XRD pattern of the NN templates. It has an orthorhombic crystal structure matched with JCPDS pattern No. 00-033-1270 for orthorhombic $NaNbO_3$ (space group: $Pbcm$). Some of the NN templates may also contain a cubic phase (JCPDS pattern No. 01-075-2102). Miller indices with subscript 'o' correspond to the orthorhombic phase, while indices with subscript 'c' correspond to the cubic phase. Cubic miller indices have a strong (*h*00) orientation, which is good for the texturing process because (*h*00) is the preferred grain orientation. Since single crystals oriented in the [001] direction as compared to other polarization directions such as [111] show improved performance [18,34,48–50], it is the most widely used method to determine the extent of texture development. In this approach, the sum of intensities of the (*h*00) peaks and the sum of all (*hkl*) peaks, including (*h*00), are calculated. The ratio of these sums provides the degree of orientation for a textured sample, with (*h*00) peak intensities increasing compared to a randomly oriented sample. The following formula is used to calculate $f_{(h00)}$:

$$f_{(h00)} = (P_{(h00)} - P_0)/(1 - P_0) \quad (3)$$

where $P_{(h00)}$ is the ratio of the sum of the intensities of all (*h*00) reflections to the sum of the intensities of all (*hkl*) reflections for the textured sample. P_0 is the ratio of the sum of the

XRD patterns of an untextured sample and textured samples with 1 wt%, 3 wt%, 5 wt%, 7 wt%, and 9 wt% template mayonnaise sintered at 1200 °C for 12 h are shown in Figure 4a. All patterns can be indexed with JCPDS pattern No. 01-075-2102 for cubic $(Na_{0.5}Bi_{0.5})TiO_3$. The Lotgering factors of these samples are calculated using their XRD patterns. The Lotgering factor ($f_{(h00)}$) is a straightforward method to quantitatively calculate texture formation [46]. Although it may overestimate the degree of texture and additional information might be necessary for a comprehensive evaluation of texture formation [51], it is the most widely used method to determine the extent of texture development. In this approach, the sum of intensities of the (*h*00) peaks and the sum of all (*hkl*) peaks, including (*h*00), are calculated. The ratio of these sums provides the degree of orientation for a textured sample, with (*h*00) peak intensities increasing compared to a randomly oriented sample. The following formula is used to calculate $f_{(h00)}$:

$$f_{(h00)} = (P_{(h00)} - P_0)/(1 - P_0) \quad (3)$$

where $P_{(h00)}$ is the ratio of the sum of the intensities of all (*h*00) reflections to the sum of the intensities of all (*hkl*) reflections for the textured sample. P_0 is the ratio of the sum of the

3.3. Texture Development

XRD patterns of an untextured sample and textured samples with 1 wt%, 3 wt%, 5 wt%, 7 wt%, and 9 wt% NN template amounts sintered at 1200 °C for 12 h are shown in Figure 4a. All patterns can be indexed with JCPDS pattern No. 01-089-3109 for cubic $(Na_{0.5}Bi_{0.5})TiO_3$. The Lotgering factors of these samples are calculated using their XRD patterns. The Lotgering factor ($f_{(h00)}$) is a straightforward method to quantitatively calculate texture formation [46]. Although it may overestimate the degree of texture and additional information might be necessary for a comprehensive evaluation of texture formation [51], it is the most widely used method to determine the extent of texture development. In this approach, the sum of intensities of the (h00) peaks and the sum of all (hkl) peaks, including (h00), are calculated. The ratio of these sums provides the degree of orientation for a textured sample, with (h00) peak intensities increasing compared to a randomly oriented sample. The following formula is used to calculate $f_{(h00)}$:

$$f_{(h00)} = (P_{(h00)} - P_0)/(1 - P_0) \quad (3)$$

where $P_{(h00)}$ is the ratio of the sum of the intensities of all (h00) reflections to the sum of the intensities of all (hkl) reflections for the textured sample. P_0 is the ratio of the sum of the intensities of all (h00) reflections to the sum of the intensities of all (hkl) reflections for the untextured sample. (In both cases, the sum of the intensities of (hkl) reflections must include the intensities of all the (h00) reflections.)

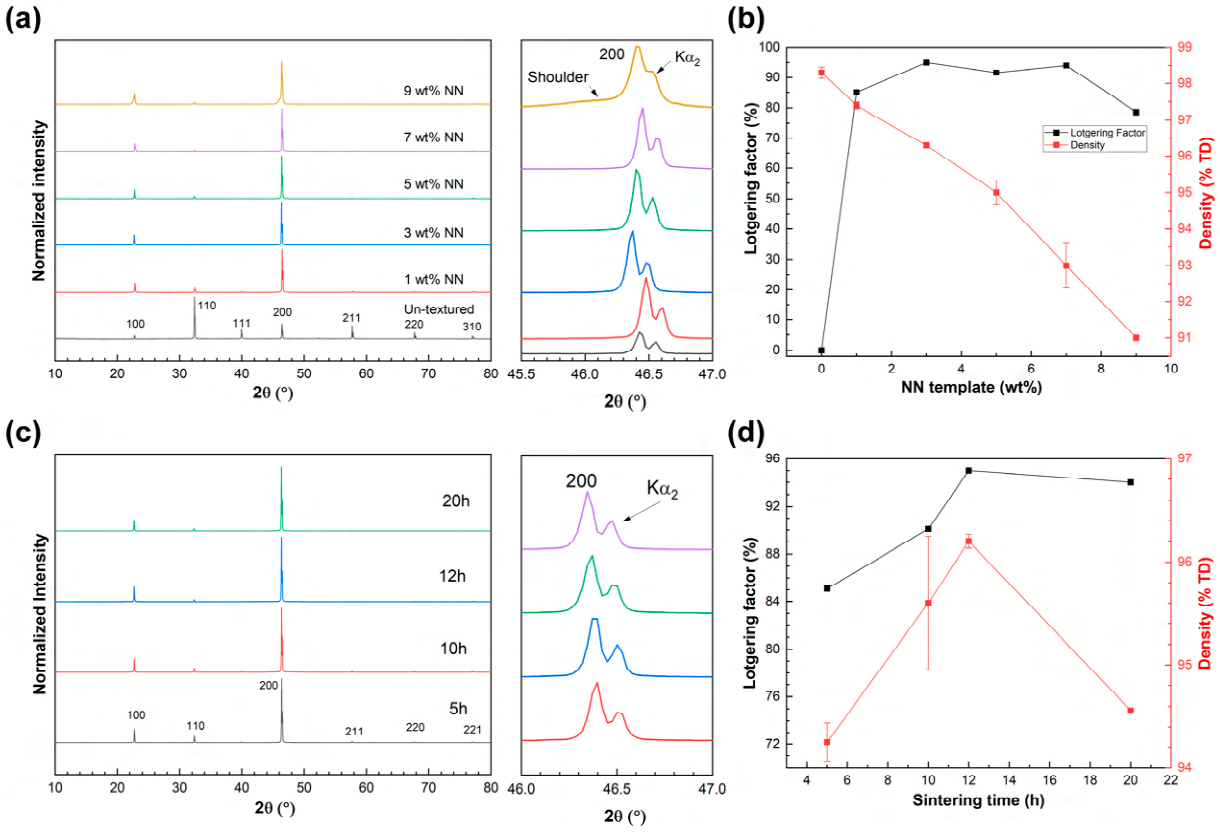

Figure 4. XRD patterns and their magnified view of (**a**) samples with different NN template content sintered at 1200 °C for 12 h; (**c**) 3 wt% NN template samples sintered for different times at 1200 °C. Lotgering factor f and relative density plots as a function of (**b**) NN template content; (**d**) sintering time (3 wt% NN template samples).

3.4. Microstructure

All samples with different NN template content show pure perovskite structure without any secondary phase peaks (Figure 4a). Moreover, a magnified view of the 200 peaks shows no peak splitting except for the $K\alpha_2$ peaks [32], indicating a pseudo-cubic structure with the texturing and density trends described above. The observed microstructure of the untextured and textured samples in Figure 5 aligns with the texturing and density trends described above. The microstructure of the untextured specimens (12 h sintering time) exhibits a highly dense structure with randomly oriented grains and a non-uniform grain size distribution. Small matrix grains ~2 μm in diameter coexist with larger abnormal grains up to ~10 μm in diameter (Figure 5a,b). In the textured sample (3 wt% NN templates, 12 h sintering time), most template particles are aligned in the casting direction, indicating successful processing. The templates ap-

for all the NN template textured specimens. The intensity of (*h*00) peaks increased, showing an improved orientation in the (*h*00) crystallographic planes. A maximum Lotgering factor of 95% is achieved for 3 wt% NN template content (Figure 4b), which is higher than that achieved in other NBT-based systems [35–37,39,52–55] and equivalent to that of the samples prepared by Ahn et al., but with a lower template amount [42]. Non-(*h*00) peaks almost disappeared except for (110), exhibiting strong orientation in the preferred direction. In the sample with 9 wt% NN templates, the 200 and 100 peaks have a shoulder on the low-angle side. NBT-BT ceramic samples have been found to contain a surface layer of ~20 mm thickness with a different structure (tetragonal or rhombohedral) to the bulk phase, which may be the cause of these shoulders [56,57].

Figure 4b shows the trends in Lotgering factor $f_{(h00)}$ and relative density (RD) with increasing template content. The theoretical density was calculated to be 5.728 g/cm^3, based on unit cell parameters obtained from XRD of a sintered pellet. Increasing the template amount enhances texturing since a larger number of template particles consume smaller grains. However, $f_{(h00)}$ does not continue to increase with higher amounts of templates because the accumulation of templates hinders oriented grain growth and causes impingement of templates. The Lotgering factor for the sample with 9 wt% NN template content drops to 78.6%. This is due to the shoulders on the 200 and 100 peaks [56,57]. If we consider the shoulders to be (00*l*) peaks of a tetragonal phase and add their intensity to the intensity of the (*h*00) peaks, then the Lotgering factor increases to 93.3%. This is close to the value of the Lotgering factor obtained (92.4%) if the shoulders are ignored. The penetration depth of X-rays into the surface of NBT-BT was estimated to be between 4.5 and 11 mm [56], so the obtained XRD pattern is sensitive to the condition of the surface. Relative density is highest for the randomly oriented sample. For the textured samples, density values continuously decrease as the number of pores increases in the sintered sample due to the anisotropy of the grains, and composition changes with the introduction of the templates (the density of orthorhombic and cubic $NaNbO_3$ is calculated in JCPDS patterns 00-033-1270 and 01-075-2102 to be 4.57 g/cm^3). Nevertheless, RD remained higher than 90% for all specimens.

Figure 4c shows the XRD patterns of 3 wt% NN template textured ceramics for various sintering times and the magnified view of the 200 reflections. There is no peak splitting except for the Kα_2 peaks. Samples were sintered for 5 h, 10 h, 12 h, and 20 h to determine the optimal time for achieving the highest grain orientation and relative density. All samples show pure perovskite structure. It was observed that the degree of texture initially increased with increasing sintering time but then slightly decreased after prolonged sintering for 20 h (Figure 4d). A sintering time of 12 h was found to be effective in inducing optimal grain orientation and density in the 3 wt% NN template textured samples. The relative density followed a similar trend. The decrease in relative density at 20 h could be related to the volatility of elements like Na at higher sintering temperatures for extended times [58]. A relatively lower density due to shorter sintering times can lead to uneven wetting of anisometric particles or pinning of domain walls by pores, resulting in low texture formation [59]. Nevertheless, similar to the previous results with varying NN template content, the relative density remained above 90%, which could be a contributing factor to the high Lotgering factor in the sintered samples.

3.4. Microstructure

The observed microstructure of untextured and textured samples in Figure 5 aligns with the texturing and density trends described above. The microstructure of the untextured specimens (12 h sintering time) exhibits a highly dense structure with randomly oriented grains and a non-uniform grain size distribution. Small matrix grains ~2 µm in diameter coexist with larger abnormal grains up to ~10 µm in diameter (Figure 5a,b). In the textured sample (3 wt% NN templates, 12 h sintering time), most template particles are aligned in the casting direction, indicating successful processing. The templates appear as rectangular-shaped depressions in the grains. This could be an effect of thermal etching, as the templates

are also visible in the polished and un-etched sample but without depression (Figure 6b).

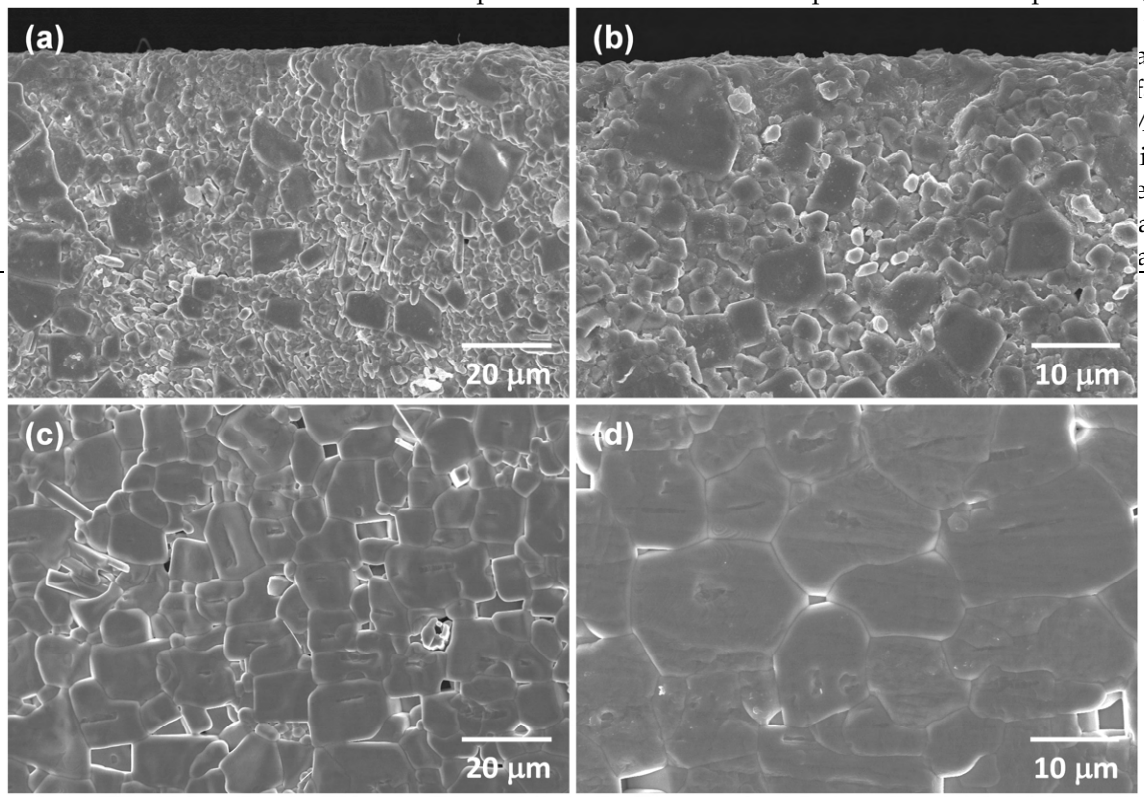

Figure 5. SEM micrographs of cross-sections of: (**a**,**b**) polished and thermally etched non-textured (12 h sintering time) samples; (**c**,**d**) textured (3 wt % $NaNbO_3$ templates 12 h sintering time) samples.

Figure 6a shows the EPMA elemental distribution in the 3 wt% NN template textured sample. All the elements except for Nb and Na are evenly distributed in the matrix outside the template regions. Na, Nb, and O are enriched inside the templates, and there are no apparent traces of Nb outside the template regions. There might be a small amount of diffusion of Nb from the templates to the 0.685NBT-0.065BT-0.25ST grains, as can be seen in the EPMA analysis. Overall, the results exhibit that the NN templates are quite stable in the 0.685NBT-0.065BT-0.25ST matrix. Figure 6b shows an SEM secondary electron mi-

Figure 5. SEM micrographs of cross-sections of: (**a**,**b**) polished and thermally etched non-textured (12 h sintering time) samples; (**c**,**d**) textured (3 wt % $NaNbO_3$ templates 12 h sintering time) samples.

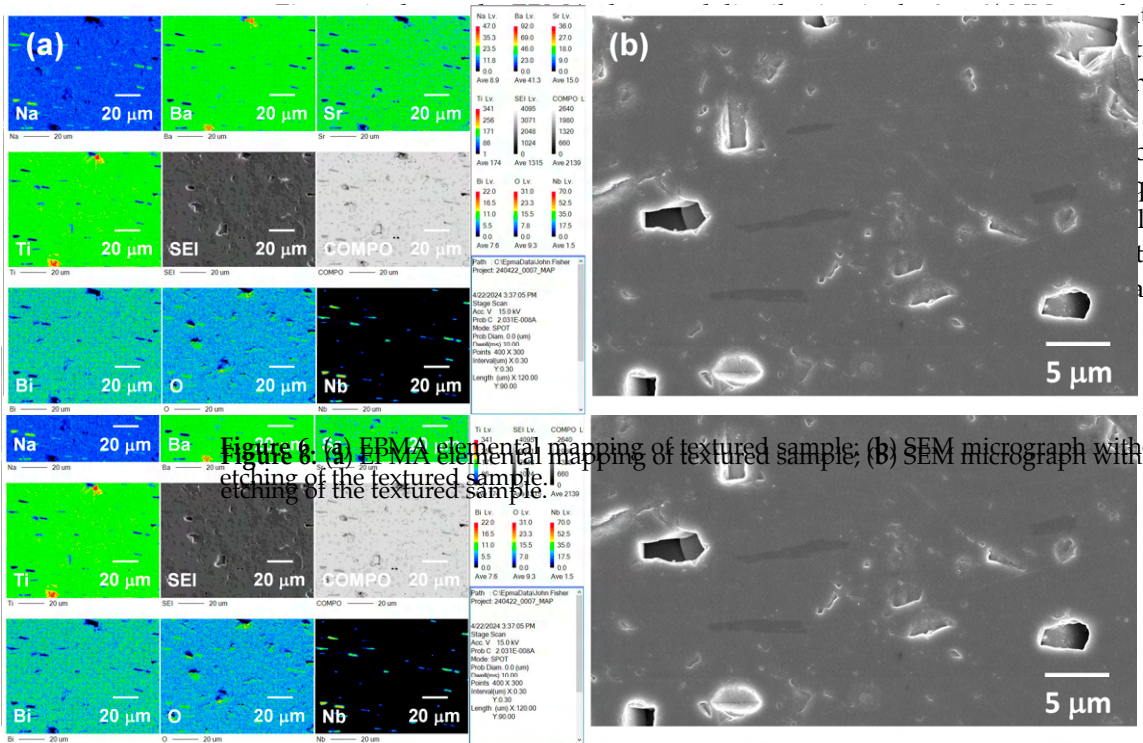

Figure 6. (a) EPMA elemental mapping of textured sample; (b) SEM micrograph without thermal etching of the textured sample.

Figure 6. (a) EPMA elemental mapping of textured sample; (b) SEM micrograph without thermal etching of the textured sample.

Figure 6a shows the EPMA elemental distribution in the 3 wt% NN template textured sample. All the elements except for Nb and Na are evenly distributed in the matrix outside the template regions. Na, Nb, and O are enriched inside the templates, and there are no apparent traces of Nb outside the template regions. There might be a small amount of diffusion of Nb from the templates to the 0.685NBT-0.065BT-0.25ST grains, as can be seen in the EPMA analysis. Overall, the results exhibit that the NN templates are quite stable in the 0.685NBT-0.065BT-0.25ST matrix. Figure 6b shows an SEM secondary electron micrograph of a polished 3 wt% NN template textured sample without thermal etching. The $NaNbO_3$ templates are visible inside some of the 0.685NBT-0.065BT-0.25ST grains.

3.5. EPMA Analysis

Table 2 presents the EPMA analysis of non-textured and 3 wt% NN template textured samples sintered at 1200 °C for 12 h. The number of moles of each element is normalized to 1 mole of B-site atoms, assuming that Nb and Al enter the perovskite B-site. The results indicate a slightly Bi-rich composition with a deficiency in Na for the non-textured sample and a slight deficiency in both Na and Bi for the textured sample. A slight deficiency is observed for Ba and Sr content in both samples. A minor deficiency in the total A-site cation amount is observed for both samples. The Bi and Na deficiency arises in NBT-based systems from their evaporation at high sintering temperatures [61,62]. While non-stoichiometry in NBT-based systems does not drastically affect the crystal structure [63], it can influence microstructure, as well as ferroelectric, dielectric, and electrostrictive properties [62–65].

Table 2. EPMA analysis of untextured and textured $0.685(Na_{0.5}Bi_{0.5})TiO_3$-$0.065BaTiO_3$-$0.25SrTiO_3$ samples.

Untextured 0.685NBT-0.065BT-0.25ST				Textured 0.685NBT-0.065BT-0.25ST		
Element	**Nominal**	**Mean**	**Standard Deviation**	**Nominal**	**Mean**	**Standard Deviation**
Na	0.3425	0.294	±0.007	0.3425	0.311	±0.049
Bi	0.3425	0.352	±0.009	0.3425	0.340	±0.032
Ti	1	0.999	±0.001	1	0.983	±0.008
Sr	0.25	0.242	±0.007	0.25	0.239	±0.009
Nb	-	not measured	-	-	0.018	±0.005
Ba	0.065	0.064	±0.003	0.065	0.063	±0.006
Al	-	0.001	±0.001	-	0.001	±0.001

The compositions of both samples align closely with the range proposed by Zhang et al. i.e., $(Na_{0.5-3x}Bi_{0.5+x})TiO_3$, where charge imbalance is mitigated [64]. If the charge is balanced and Na loss is fully compensated by Bi excess, no oxygen vacancies should occur. In the non-textured NBT-BT-ST sample, Bi exceeds the nominal value by x = 0.0095. Thus, according to the proposed composition range, our composition (excluding Aluminum) should be $(Na_{0.3278}Bi_{0.3519}Ba_{0.0622}Sr_{0.2393})TiO_3$. However, the actual compositions observed in EPMA analysis are even more Na-deficient, indicating significant Na loss during sintering. In the textured sample, Nb is found in the matrix, indicating a minor diffusion of template elements into the matrix. Aluminum is also detected in both samples, albeit in very small amounts, likely due to contamination from the alumina crucible. Furthermore, it is not evenly distributed in the samples, as it is found at only a few analysis points.

3.6. Polarization and Strain vs. Electric Field Hysteresis Loops

For polarization and strain vs. electric field measurements, one untextured and three 3 wt% NN template textured samples were measured. The first textured sample (called sample T1) suffered an electrical breakdown during bipolar polarization and strain vs. electric field measurements, so two identical replacement textured samples (called sample T2) were also measured. The XRD patterns of the two textured samples indicate that they have differences in structure. The XRD pattern of sample T1 (Figure 7a) has a pseudocubic

structure as previously described. The XRD pattern of sample T2 shows low-angle shoulders on the 200 and 100 reflections (Figure 7b). The shoulders are more pronounced than the low-angle shoulders seen in the 9 wt% NN template textured sample (Figure 4a). If the shoulders are treated as tetragonal (00*l*) peaks and their intensity is included with the (*h*00) peaks, the Lotgering factor is 94.9%, similar to that of the sample shown in Figure 4. If the shoulders are treated as non-(*h*00) or non-(00*l*) peaks, then the Lotgering factor drops to 56.8%. The pattern looks similar to XRD patterns of poled NBT-based materials, in which an additional tetragonal or rhombohedral phase appears, although the samples were not poled [66,67]. Sample T2 may, therefore, contain an additional rhombohedral or tetragonal phase in addition to the pseudocubic phase, as mentioned earlier [56,57]. The increase in the intensity of the shoulders may be caused by Bi deficiency [56,57].

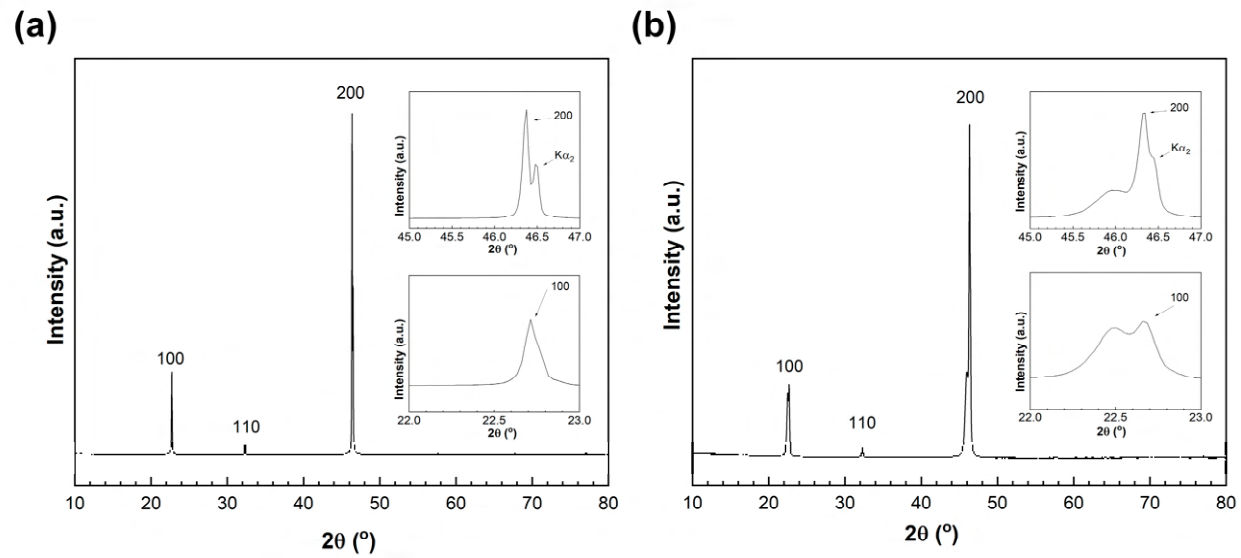

Figure 7. XRD patterns of 3 wt% NN template textured samples (**a**) T1 and (**b**) T2.

Figure 8 shows bipolar polarization and strain vs. electric field hysteresis loops for the untextured and textured samples. All three samples show slim polarization hysteresis loops typical for a relaxor material (Figure 8a–c) [13,68,69]. The loops have a pinched appearance characteristic of an antiferroelectric or incipient ferroelectric material [4,20,24,31,32,70,71]. The textured samples have slimmer polarization hysteresis loops than the untextured sample, reflecting an orientation dependence of ferroelectric properties [34,72]. The textured sample T1 suffered a dielectric breakdown during measurement at an electric field of 3 kV/mm. The bipolar strain hysteresis loops for the untextured and textured (sample T1) samples have a sprout shape characteristic of an antiferroelectric or incipient ferroelectric material, while textured sample T2 has much slimmer loops characteristic of an electrostrictive material [18,31,32,73–75]. The 0.685NBT-0.065BT-0.25ST composition appears to be at the boundary between incipient ferroelectric and electrostrictive behavior. The textured samples have considerably higher electric field-induced strains than the untextured sample. Sample T1, which suffered a dielectric breakdown during measurement, has a maximum strain of 0.06% at an electric field of 3 kV/mm, while the untextured sample has a maximum strain of 0.01% at the same electric field. Textured sample T2 has even higher strains, with a strain of 0.12% at an electric field of 3 kV/mm and a maximum strain of 0.21% at an electric field of 4 kV/mm.

Figure 9 displays room temperature polarization, current density, and strain hysteresis loops for untextured and 3 wt% NN textured samples at an electric field of 4 kV/mm. Both samples exhibit slim polarization hysteresis loops characteristic of relaxor behavior (Figure 9a). The polarization hysteresis loop of the textured sample shows a slightly pinched characteristic due to a decrease in remanent polarization (P_r). P_r and coercive field (E_c) are 1.88 μC/cm^2 and 0.34 kV/mm for the textured sample and 3.11 μC/cm^2 and 0.49 kV/mm

for the non-textured sample. This pinched characteristic is due to uniform crystallographic alignment [53]. It may also result from the growth of polar nano-regions (PNRs) or ionic defects, likely due to the diffusion of some elements from the template regions to the matrix during high-temperature sintering, which enhances relaxor behavior, thereby exhibiting a higher electrostrictive effect post-texturing [40,76,77]. The current density loops (Figure 9b) align with the polarization hysteresis loops, showing similar behavior for both untextured and textured samples. The current density loops lack the significant peaks which are usually observed in typical ferroelectric and electric field-induced relaxor-ferroelectric transition responses, indicating no relaxor-ferroelectric phase transition [30]; instead, the broad loop suggests a dominant non-polar phase [64]. Usually, peaks 1 and 4 (p1 and p4) correspond to ferroelectric domain switching, and peaks 2 and 3 (p2 and p3) correspond to the electric field-induced relaxor-ferroelectric phase transition [69]. When an ergodic state is pervasive, as in the current composition, a high electric field is needed to transform PNRs to a long-range FE state [78]. Therefore, there are no sharp peaks in the current density curve showing field-induced phase transition or ferroelectric domain switching. Moreover, broad peaks (p1 and p2) suggest that PNRs transform to a strongly polar state at p1 and revert to a weakly polar or relaxor state at p2 [69,75].

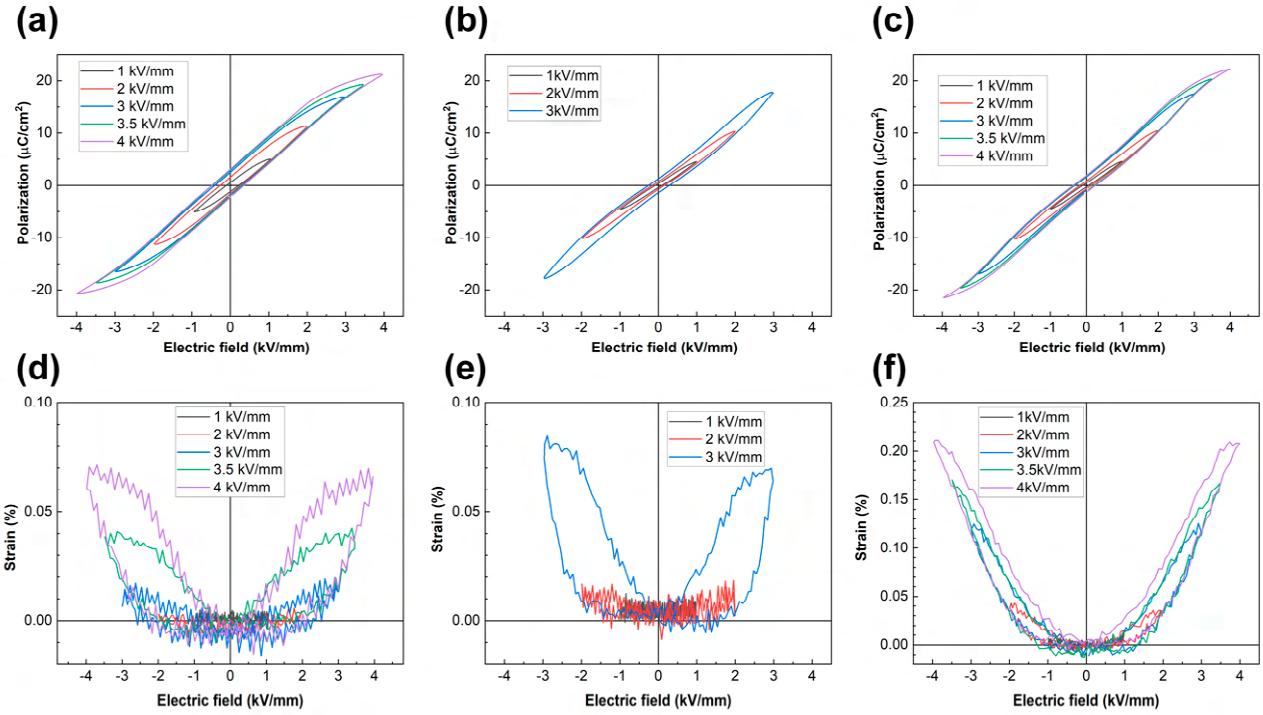

Figure 8. Polarization and strain vs. electric field hysteresis loops of (**a**,**d**) untextured; (**b**,**e**) 3 wt% NN template textured sample T1; (**c**,**f**) 3 wt% NN template textured sample T2.

A comparison of bipolar S-E loops in Figure 9c reveals that NBT-BT-ST oriented along the (001) direction generates significantly enhanced strain under the same electric field with lower hysteresis. The maximum bipolar strain is calculated as 0.21% and 0.72% for untextured and textured samples, respectively. The bipolar S-E curves remain positive regardless of the electric field direction, showing the polarization (P) is independent of the electric field. Although the coercive field (E$_c$) of the textured sample (1.88 kV/mm) is higher than that of the untextured sample (1.34 kV/mm), the remnant polarization (P$_r$) and remnant strain (S$_r$) are also higher (P$_r$ = 31 μC/cm^2 and S$_r$ = 0.49) for the textured sample. This positive characteristic is due to polarization rotation by alignment [53]. It may also result from the growth of polar nano-regions (PNRs) or ionic defects, likely due to the diffusion of some elements from the template regions to the matrix during high-temperature sintering, which enhances relaxor behavior, thereby exhibiting a higher electrostrictive effect post-texturing [40,76,77]. The current density loops (Figure 9b) align with the polarization hysteresis loops, showing similar behavior for both untextured and textured samples. The current density loops lack the significant peaks which are usually observed in typical ferroelectric and electric field-induced relaxor-ferroelectric transition responses, indicating no relaxor-ferroelectric phase transition [30]; instead, the broad loop suggests a dominant non-polar phase [64]. Usually, peaks 1 and 4 (p1 and p4) correspond to ferroelectric domain switching, and peaks 2 and 3 (p2 and p3) correspond to the electric field-induced relaxor-ferroelectric phase transition [69]. When an ergodic state is pervasive, as in the current composition, a high electric field is needed to transform PNRs to a long-range FE state [78]. Therefore, there are no sharp peaks in the current density curve showing field-induced phase transition or ferroelectric domain switching. Moreover, broad peaks (p1 and p2) suggest that PNRs transform to a strongly polar state at p1 and revert to a weakly polar or relaxor state at p2 [69,75].

Figure 8. Polarization and strain vs. electric field hysteresis loops of (a,d) untextured; (b,e) 3 wt% NN template textured sample T1; (c,f) 3 wt% NN template textured sample T2.

Figure 9 displays room temperature polarization, current, and strain hysteresis loops for untextured and 3 wt% NN textured samples at an electric field of 4 kV/mm. With samples exhibiting the polarization hysteresis loop characteristic, relaxor behavior is typically attributed to the electric field-induced transition of polar nano-regions (PNRs) to a long-range ferroelectric (FE) order [79,80]. Hysteresis can also occur if texturing is imperfect, with not all grains perfectly aligned in the (001)

direction [86]. Hysteresis decreases noticeably after texturing. Hysteretic behavior also translates into the shape of the S-P^2 curves (Figure 9d). The deviation in the S-P^2 curve from linearity indicates that the electrostrictive effect is predominant but that the strain is not purely electrostrictive [32]. The deviation from linearity is larger in the non-textured sample and greatly reduced in the textured sample. This demonstrates the effectiveness of the texturing process in bringing samples of the same composition into a nearly pure electrostrictive state without drastic compositional changes, achieved by merely inducing anisotropy in the system. The electrostrictive coefficient Q_{33} is calculated from the fitted S-P^2 curve using the equation

$$S = Q_{33}P^2 \quad (4)$$

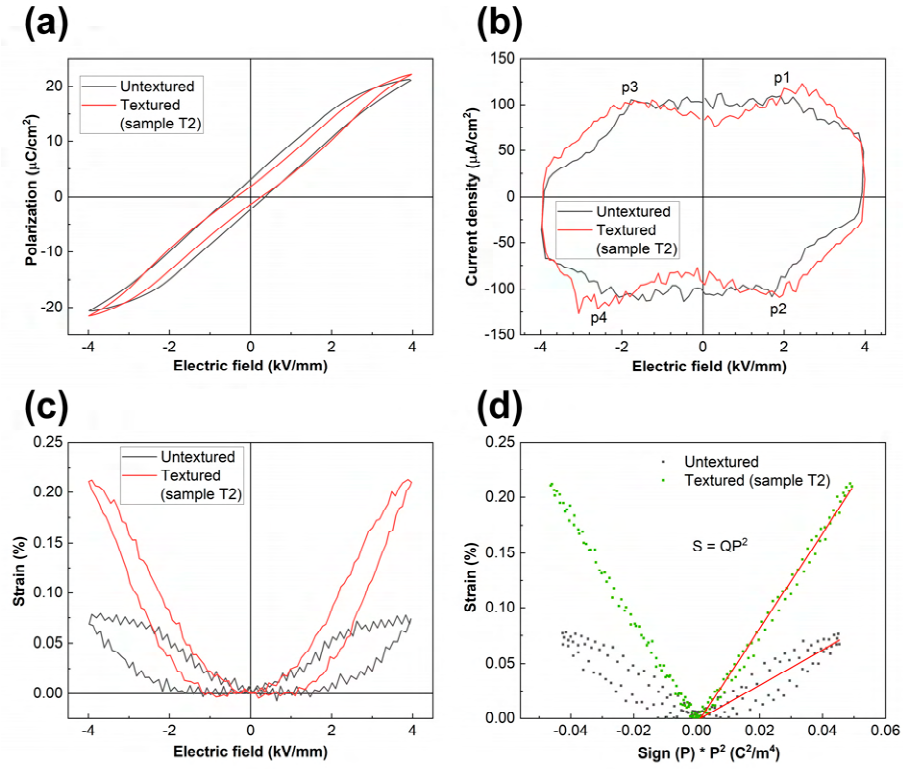

Figure 9. (**a**) Bipolar P-E loops, (**b**) current density loops, (**c**) bipolar S-E loops, (**d**) S-P^2 plots for 3 wt % textured and non-textured samples.

A comparison of bipolar S-E loops in Figure 9c reveals that NBT-BT-ST oriented along the (001) direction generates significantly enhanced strain under the same electric field with lower hysteresis. The maximum bipolar strains calculated are 0.21% and 0.12% for textured and untextured samples, respectively. The bipolar S-E curves remain positive regardless of the electric field direction, showing that electrostriction is independent of the electric field. Although the ferroelectric (FE) order is disrupted by ST addition, and the ergodic phase dominates in the composition [32], non-zero remanent polarization (P_r) results in hysteresis in the bipolar S-E loops for both textured and non-textured samples, suggesting traces of macrodomains [73,74,77,79,80] and some strain resulting from extrinsic contributions (domain wall motion) [74,81–84]. The hysteretic behavior resembles other NBT-based compositions in an ergodic state at room temperature [73,80,85]. Hysteresis can also occur if texturing is imperfect, with not all grains perfectly aligned in the (001) direction [86]. Hysteresis decreases noticeably after texturing. Hysteretic behavior also translates into the shape of the S-P^2 curves (Figure 9d). The deviation in the S-P^2 curve from linearity indicates that the electrostrictive effect is predominant but that the strain is not purely electrostrictive [32]. The deviation from linearity is larger in the non-textured sample and greatly reduced in the textured sample. This demonstrates the effectiveness of the texturing process in bringing samples of the same composition into a nearly pure electrostrictive state without drastic compositional changes, achieved by merely inducing anisotropy in the system. The electrostrictive coefficient Q_{33} is calculated from the fitted S-P^2 curve using the equation

$$S = Q_{33}P^2 \quad (4)$$

Q_{33} is calculated at 4 kV/mm because, at higher electric fields, strain is mainly due to electrostriction with little contribution from extrinsic effects [42,87]. Strain at lower electric fields can result from micro-domain (polar nanoregion) wall motion, reducing the calculated Q value [83]. The electrostrictive coefficient Q_{33} increased from 0.017 m^4C^{-2} for the non-textured sample to 0.043 m^4C^{-2}, which is higher than that of some of the NBT-based materials and PMN [24,53,66,73,79,83,88–95]. It significantly increased after fabricating the microstructure in the (*l*00) crystallographic direction due to single-crystal-like anisotropy achieved through texturing [18]; moreover, studies show that Q_{33} values recorded in the (00*l*) direction are higher than in the other crystallographic directions [83,88].

Unipolar polarization and strain vs. electric field hysteresis loops are shown in Figure 10. Unipolar polarization hysteresis loops exhibit similar behavior at various electric fields. The first T2 textured sample suffered an electrical breakdown during bipolar measurement at an electric field of 4 kV/mm, so the second T2 textured sample was used for unipolar measurements. The textured sample T2 has noticeably slimmer hysteresis loops than the untextured and textured sample T1 (Figure 10c). The unipolar strain hysteresis loops for the untextured sample and textured sample T1 appear similar to those of antiferroelectric or incipient ferroelectric materials (Figure 10a,b) [4,20,24,31,70,71,77,96], while the loops for textured sample T2 correspond to an electrostrictive material [18,32,73–75].

The maximum unipolar strain for the textured sample is 0.23% (sample T2) compared to 0.09% for the untextured sample. Unipolar strain increased by a factor of 2.56 after texturing. Hysteresis for both non-textured and textured samples is measured using the formula $H = \Delta S/S_{max}$, where ΔS is measured at $E_{max}/2$ and S_{max} is measured at E_{max}, respectively [97]. The corresponding hysteresis decreased from 44% to 16% after texturing (sample T2). Both high electrostrain and significantly low hysteresis demonstrate the effectiveness of the textured 0.685NBT-0.065BT-0.25ST system with NN templates. Since low driving field, low hysteresis, and large strains are desirable for actuator applications, S_{max}/E_{max} is calculated from unipolar strains at electric fields of 3, 3.5, and 4 k/mm for both textured and untextured samples in Figure 10d–f. Textured ceramics exhibit higher electric field-induced strain performance than randomly oriented samples at all electric fields. This implies that the textured sample requires a relatively lower electric field to induce large strain. The textured 0.685NBT-0.065BT-0.25ST samples in the present work also required noticeably lower electric fields than in previous works [24,53,66,73,79,83,88–93]. The maximum normalized strain, d_{33}^*, obtained for textured ceramics is 581 pm/V (sample T2), higher than what is obtained in untextured NBT-BT-ST [32].

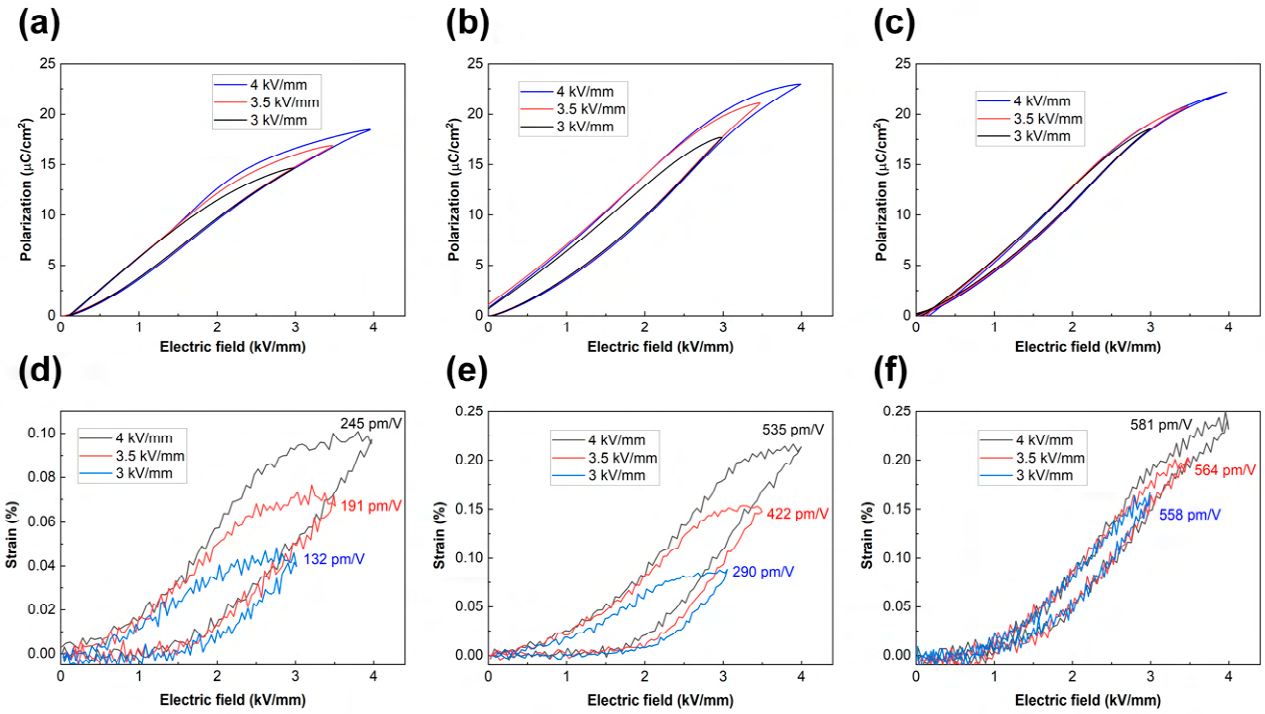

Figure 10. Unipolar polarization and strain vs. electric field hysteresis loops of (**a**,**d**) untextured; (**b**,**e**) 3 wt% NN template textured sample T1; (**c**,**f**) 3 wt% NN template textured sample T2.

3.7. Dielectric Properties

The textured samples T1 and T2 have very different inverse piezoelectric properties, as they were prepared under nominally identical conditions. It may be due to the differences in structure as determined by XRD (Figure 7). However, if the differences in structure are due to a surface layer, it may not have a large effect on the properties, as the surface layer in NBT-BT was only estimated to be ~20 µm in thickness [56]. The difference in piezoelectric properties may also be due to differences in composition due to Bi or Na evaporation. Non-stoichiometry has been shown to affect the structure, microstructure, and piezoelectric properties of untextured NBT ceramics [62,98,99]. Sintering at a lower temperature may be beneficial in reducing Bi and Na evaporation, although this would be offset by the need for longer sintering times to achieve the same degree of texturing and densification. Another possibility is differences in the degree of NN template alignment between different samples. It can be seen in Figure 5c that some of the templates and grains are misaligned. Further experiments to optimize the tape-casting conditions (doctor blade

Temperature-dependent AC responses were measured on cooling from 550 °C ~195 °C for untextured (Figure 11) and 3 wt% NN template textured (Figure 12) samples. The data at selected frequencies of Log(f/Hz) = 5 to 1.5 with an interval of 0.5 are shown. (Higher frequencies of 5.5 and 6.0 are strongly affected by the stray effects and thus are not shown). Relative permittivity values are shown in Figures 11a and 12a in linear and logarithmic scale. The dispersive behavior around room temperature shows that the samples contain polar nanoregions (PNRs) [33,100] as discussed above.

The relative permittivity plots of NBT-based materials typically show frequency-dependent or dispersive shoulders at lower temperatures (marked T_s) and a frequency-independent maximum (marked T_m) [31,32,69,100], but with a high level of component addition (such as ST addition in NBT-BT-ST), the value of relative permittivity at T_m decreases relative to T_s, as is the case here [22,69,74,92], resulting in the frequency-dependent peaks at T_s and the peak at T_m becoming indistinguishable. The frequency-independent or weakly dependent broad peak at T_m and the frequency-dependent 'shoulder' at T_s indicate relaxor behavior in NBT-type compositions [69,100,101]. It has been proposed that T_m is related to the thermal evolution of relaxation time or correlation length distribution of tetragonal PNRs that emerged from the rhombohedral phase and that the peak does not

height and casting speed) may help to reduce variation in the degree of texturing between different samples. The textured samples are also more prone to electrical breakdown than the untextured samples, probably due to the larger grain size and lower density. Further work needs to be carried out to improve reproducibility of the sample properties.

3.7. Dielectric Properties

Temperature-dependent AC responses were measured on cooling from 550 °C~−193 °C for untextured (Figure 11) and 3 wt% NN template textured (Figure 12) samples. The data at selected frequencies of Log(f/Hz) = 5 to 1.5 with an interval of 0.5 are shown. (Higher frequencies of 5.5 and 6.0 are strongly affected by the stray effects and thus are not shown). Relative permittivity values are shown in Figures 11a and 12a in linear and logarithmic scale. The dispersive behavior around room temperature shows that the samples contain polar nanoregions (PNRs) [33,100] as discussed above.

Table 3. Parameters for temperature-dependent permittivity, inverse permittivity, loss tangents, and conductivity. Asterisks indicate the low-temperature region.

Parameter	T_d	$T_{s\text{-}m}$	T_θ	T_B	A	B/B *	$T_{4.5}/T_{4.5}$ *	T_2/T_2 *	C/C *	D	E_a
Unit	°C	°C	°C	°C	$°C^{-1}$	$°C^{-1}$	°C	°C	°C	$\ln(\Omega^{-1}cm^{-1}K)$	eV
Untextured	−35	150	260.7	437	0.00326	0.00652 (=2A) 0.02363	98.65 −34.36	71.50 −53.62	10.86 7.70	8.1	1.26
Textured	−32	135	239.6	452	0.00395	0.00790 (=2A) 0.02560	92.96 −29.73	67.17 −48.04	10.32 7.32	7.7	1.23

The relative permittivity plots of NBT-based materials typically show frequency-dependent or dispersive shoulders at lower temperatures (marked T_s) and a frequency-independent maximum (marked T_m) [31,32,69,100], but with a high level of component addition (such as ST addition in NBT-BT-ST), the value of relative permittivity at T_m decreases relative to T_s, as is the case here [22,69,74,92], resulting in the frequency-dependent peaks at T_s and the peak at T_m becoming indistinguishable. The frequency-independent or weakly dependent broad peak at T_m and the frequency-dependent 'shoulder' at T_s indicate relaxor behavior in NBT-type compositions [69,100,101]. It has been proposed that T_m is related to the thermal evolution of relaxation time or correlation length distribution of tetragonal PNRs that emerged from the rhombohedral phase and that the peak does not correspond to any phase transition [101]. T_s is also related to the thermal evolution of discrete PNRs, and no phase transition occurs here [101]. The thermal evolution of an initially existing mixture of *R*3*c* rhombohedral and *P*4*bm* tetragonal PNRs results in T_s [22,69,74,90,101]. The rhombohedral PNRs transition to tetragonal PNRs in the temperature range between the two maxima.

As both T_s and T_m are poorly defined, $T_{s\text{-}m}$ is chosen as the boundary between the regions of dispersive and non-dispersive behavior around 150 °C and 135 °C for the untextured and textured samples, respectively. Textured samples exhibit substantially lower permittivities around $T_{s\text{-}m}$ and near room temperature, as also reported previously [41], which is also qualitatively consistent with the behavior of the P-E hysteresis loops in Figure 9. In Figure 9a, from the slope at low field, the dielectric constants for untextured and textured samples are estimated as 7230 and 5960, respectively, which are indicated as star symbols in Figures 11a and 12a. From the dispersive behavior around room temperature, the dielectric constants estimated from the P-E loops may be considered to be low-frequency, DC limit values. Although the frequency dispersion (or dependence) appears to be decreased at low temperatures in linear scale [Figures 11a and 12a], they are comparable, as shown in the logarithmic scale plots in Figures 11b and 12b, lower. In fact, well-structured frequency dispersion can be seen in the reciprocal permittivity plots, $1/\varepsilon'$,

as recently introduced for KNN-based samples [102,103], shown in Figures 11b and 12b. For the dispersive behavior below $T_{s\text{-}m}$, the reciprocal permittivity at different frequencies is in parallel, regularly shifted by the logarithmic frequencies as

$$1/\varepsilon\prime = -B\left(T - T_f\right) \quad (5)$$

$$T_f = T_{4.5} - C\,(4.5 - \mathrm{Log}f) \quad (6)$$

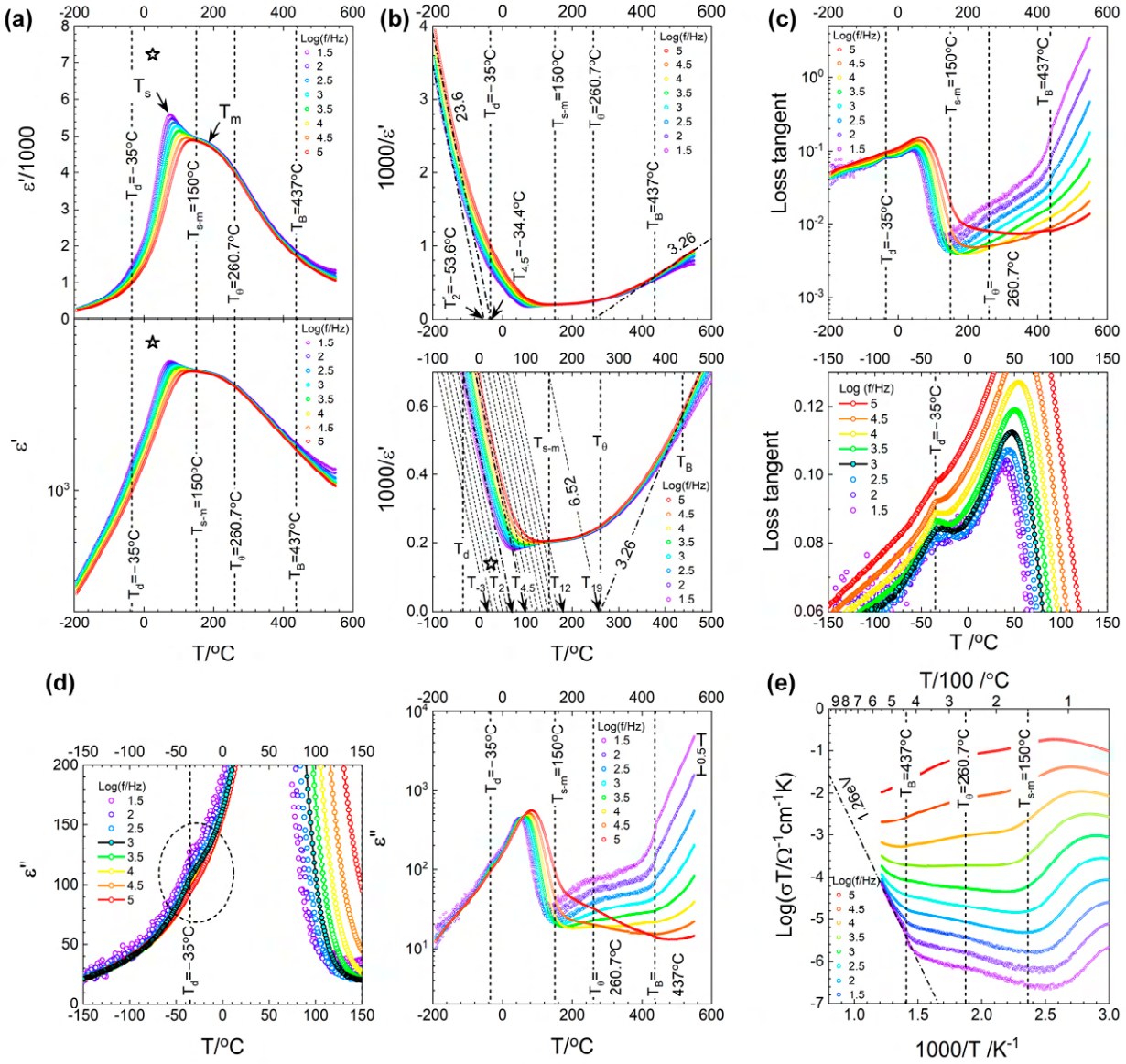

Figure 11. Dielectric and AC conductivity properties of the untextured sample tested for frequencies over the temperature range of 50 °C–550 °C measured on cooling: (**a**) temperature dependence plots of relative (real) permittivity in linear and logarithmic scale; (**b**) the reciprocal permittivity in a full and low range; (**c**) loss tangents in logarithmic and a magnified linear scale; (**d**) the imaginary permittivity in a magnified linear scale and in the logarithmic scale; (**e**) the Arrhenius plots of the AC conductivity. The characteristic temperatures and the slopes are indicated (see Table 3). The star symbol represents the dielectric constant estimated from the P-E hysteresis loop (Figure 9).

As both T_s and T_m are poorly defined, $T_{s\text{-}m}$ is chosen as the boundary between the regions of dispersive and non-dispersive behavior around 150 °C and 135 °C for the untextured and textured samples, respectively. Textured samples exhibit substantially lower permittivities around $T_{s\text{-}m}$ and near room temperature, as also reported previously [41], which is also qualitatively consistent with the behavior of the P-E hysteresis loops in Figure 9. In Figure 9a, from the slope at low field, the dielectric constants for untextured and textured samples are estimated as 7230 and 5960, respectively, which are indicated as star symbols in Figures 11a and 12a. From the dispersive behavior around room temperature,

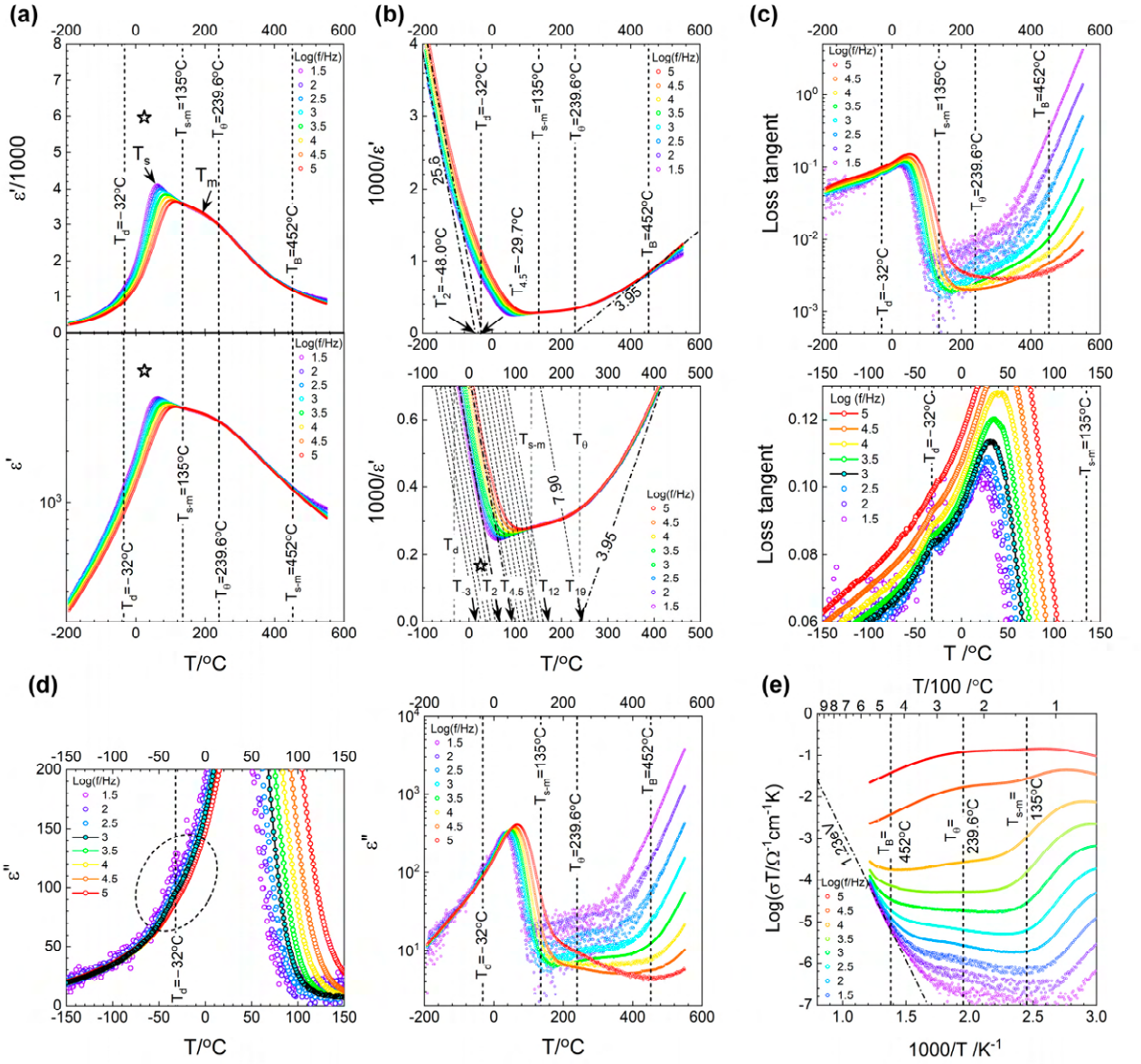

Figure 12. Dielectric and AC conductivity properties of a 3 wt% NN template textured sample at selected frequencies over the temperature range of 550 °C~−193 °C measured on cooling: (**a**) temperature dependence plots of relative (real) permittivity in linear and logarithmic scale; (**b**) the reciprocal permittivity in a full and low range; (**c**) loss tangents in logarithmic and a magnified linear scale; (**d**) the imaginary permittivity in a magnified linear scale and (**e**) the Arrhenius plots of the AC conductivity. The characteristic temperatures and the slopes are indicated (see Table 3). The star symbol represents the dielectric constant estimated from the P-E hysteresis loop (Figure 9).

In the upper and lower graphs, two different slopes are estimated below and above −50 °C as indicated by dot-dashed lines. The lines, with identical slope 3, and *x*-axis intercept *T*$_2$ with the frequency dependence (*T*$_{4.5}$ is estimated from the data at Log(*f*/Hz) = 4.5 and 2, are significant variations in temperature. The magnified view in the linear scale in the lower graph is at Log(*f*/Hz) = 4.5 and 2 and the errors are smaller than the symbols.

So far, only the real part of complex permittivity has been discussed. A standard representation of the temperature dependence of the dielectric properties is to present the loss tangent, tan δ, as shown in Figures 11 and 12c. It is presented that Log(*f*/Hz) = 4.5 and 2, and significant variations in temperature. The magnified view in the linear scale in the lower graph is at Log(*f*/Hz) = 4.5 and 2 and the errors are smaller than the symbols. The loss tangent provides a good indication of the dielectric losses in the ferroelectric and paraelectric regions. In the ferroelectric region, it is presented by the plateau-like peaks, a *B*-anomaly, at the Curie–Weiss temperature, *T*$_θ$ [95]. Its peak value is approximately 0.0234 °C^{-1} and 0.0256 °C^{-1} at *T*$_θ$ = 239.6 °C and *T*$_{s-m}$ = 135 °C, respectively. The dielectric constant and the dielectric loss curve, the shift with log(*f*/Hz) as well as the depolarization temperature and texturing will be discussed in more detail in Section 3.7 and 3.8. For unpoled samples, the textured sample [32] has a slightly stronger temperature dependence and higher temperature, but the frequency dependence is very similar. From the similar analysis for the

temperature range from −40 to 30 °C, shown in the lower graphs of Figures 11b and 12b, B are estimated as 0.00652 °C^{-1} and 0.00790 °C^{-1}, T_f as 98.7 and 93.0 °C, and C, the shift with logarithmic frequency, as 10.9 and 10.3 °C for untextured and textured samples. The temperature dependence is shown to be double that for the Curie–Weiss behavior,

$$1/\varepsilon' = A(T - T_\theta) \tag{7}$$

i.e., $B = 2A$ where A are estimated as 0.00326 °C^{-1} and 0.00395 °C^{-1}, T_θ as 260.7 and 239.6 °C, reminiscent of the "two" law known for the 1st and 2nd order ferro-paraelectric transitions [104,105]. To the authors' knowledge, this temperature dependence as such has not been reported for relaxor-like materials. The plots for the higher and lower frequencies can be simulated from the constants in Table 3, as indicated by dashed lines in Figures 11b and 12b, lower. It is interesting to note that for frequencies above 1 THz (10^{12} Hz), the plots appear above $T_{s\text{-}m}$ in the non-dispersive region. These frequencies are relevant for Raman spectra of the vibrational phonon modes responsible for the phase transitions for NBT in the wavenumber region 100~600 cm^{-1} [34], corresponding to frequencies between 3 and 18 THz. If the plot meets the plot for the Curie–Weiss behavior at T_θ for the non-relaxor ferroelectrics, the corresponding frequency should be above 10^{19} Hz, in the frequency range of gamma rays. The dielectric constants estimated from the P-E loops, marked by the star symbols, are now more probably located as a lower frequency response. Dielectric peaks that increase by more than one order of magnitude were previously observed at low frequencies, such as from 0.01 Hz to 100 Hz, in relaxor materials [106]. The temperature-frequency dependence of the relaxor-like behavior observed in this work requires investigations by theoretical physicists.

So far, only the real part of complex permittivity has been discussed. A standard presentation of the temperature dependence of the dielectric properties is to present the loss tangent, tan δ, as shown in Figures 11c and 12c. It is presented in the logarithmic scale to show significant variations in temperatures. In the magnified view in the linear scale in the lower graphs, tan δ plots reveal a frequency-independent peak at −35 and −32 °C, corresponding to the depolarization temperature T_d [95]. For poled samples, it appears as a vertical step in the dielectric constant curve and as a peak in the dielectric loss curve at all frequencies [12,13,19,32,101,107]. Since the depolarization temperature T_d is well below room temperature [32] the composition is in an ergodic state at room temperature for both textured and untextured samples.

The effect is more clearly shown at lower frequencies, but as the noise becomes large, the data at 10^3 Hz is emphasized to explain the behavior. The depolarization temperature roughly corresponds to the transition between different temperature dependences, B^* and B but the $1/\varepsilon'$ plots cannot explain the transition or the peak localized at T_d. The temperature and frequency dependence are difficult to understand as $\tan\delta = \frac{\varepsilon''}{\varepsilon'}$ the ratio of ε'' over ε', even with the $1/\varepsilon'$ presentation in Figures 11b and 12b. The imaginary dielectric constant, shown in Figures 11d and 12d, can explain the tan δ plots. ε'' shows frequency-dependent peaks T_s but rapidly and strongly decreases by more than one order of magnitude by $T_{s\text{-}m}$. The peaks are better distinguished in plots of ε'' than in ε'. Arrhenius plots of frequency and loss peak temperature give activation energies of 2.3 and 1.9 eV for untextured and textured samples, respectively.

$$\ln f = D - E_s/k_B T_s \tag{8}$$

The frequency and temperature dependence above $T_{s\text{-}m}$ in tan δ comes essentially from ε''. In contrast, well below T_d, ε'' does not show any frequency dispersion. The frequency dispersion in tan δ is essentially that of $1/\varepsilon'$. A small dispersion starting below T_d explains the more discernible peaks at T_d in tan δ with the baseline compensated by $1/\varepsilon'$.

It is also interesting to note that the Curie–Weiss temperature T_θ, and the Burns temperature, T_B, estimated from the deviation in the Curie–Weiss behavior as 437 and 452 °C, for untextured and textured samples in Figures 11b and 12b mark the transitions in

ε'' more predominantly than in ε'. Above T_B, the material is completely paraelectric. As emphasized recently [34,103,108,109], Arrhenius conductivity appears in the paraelectric phase. Here, above T_B, the strong temperature and the frequency dependence as $\varepsilon'' \propto 1/f$ at low frequencies, corresponds to the dc conductivity, σ_{dc} since

$$\sigma' = (2\pi f)\varepsilon'' \tag{9}$$

The Arrhenius plots of $\sigma'(f)T$ in Figures 11e and 12e show the activation energies of 1.26 and 1.23 eV,

$$\ln \sigma_{\mathrm{dc}} T = E - E_{dc}/k_{\mathrm{B}}T \tag{10}$$

which is likely to represent hole conduction.

4. Conclusions

This study investigated the texturing effect on the predominantly electrostrictive composition $0.685(Na_{0.5}Bi_{0.5})TiO_3$-$0.065BaTiO_3$-$0.25SrTiO_3$, aiming to enhance its electrostrictive properties. Samples with a high degree of orientation (Lotgering factor of 95%) were prepared by templated grain growth using 3 wt% of $NaNbO_3$ templates. Textured and untextured compositions showed dielectric property behavior typical of $(Na_{0.5}Bi_{0.5})TiO_3$-based relaxor materials. Both textured and untextured compositions displayed an ergodic relaxor phase with slim polarization hysteresis loops. After texturing, unipolar strain increased from 0.09% for untextured ceramics to 0.23% for textured ceramics, an increase of a factor of 2.56. A high normalized strain of 581 pm/V at an electric field of 4 kV/mm was achieved for the textured sample, with significant improvements in S_{max}/E_{max} at electric fields between 3 and 4 kV/mm compared to the untextured sample. This study shows that the same composition exhibited significantly improved electromechanical properties after texturing. A large electrostrictive coefficient, Q_{33}, of 0.043 m^4C^{-2} was achieved for the textured ceramic at a relatively low electric field of 4 kV/mm, accompanied by a substantial decrease in strain hysteresis from 44% in untextured samples to 16% in the textured sample. These results demonstrate that grain orientation plays a crucial role in enhancing electrostrictive and electromechanical properties, making textured ceramics suitable for application in actuation devices. Dielectric measurements over a wide temperature range from −193 to 550 °C confirmed the ergodic state at room temperature with dispersive dielectric constants below ca. 150/130 °C for untextured/textured samples. The "two" law, double the Curie–Weiss constant, was found in the temperature dependence of inverse dielectric constants, which shifts by ca. 10 °C per decade and thus suggests the limiting THz Raman interaction and explains the dielectric constant values estimated from the P-E hysteresis loops. Dielectric loss is only a little dispersive at low temperatures and indicates the depolarization temperature around −35/−32 °C. The loss peak dispersion indicates the activated transitions of polar nanoregions with activation energies of 2.3/1.9 eV. Above the Burns temperature at 437/452 °C, dc loss with activation energies ~1.26/1.23 eV is evidenced.

Author Contributions: Conceptualization, J.G.F.; Data curation, K.A.; Formal analysis, K.A. and J.-S.L.; Funding acquisition, J.G.F. and J.-S.L.; Investigation, K.A., D.T.T., T.T.H.T. and W.-J.C.; Methodology, J.G.F.; Project administration, J.G.F. and J.-S.L.; Resources, J.G.F., T.T.H.T., J.-S.L. and W.J.; Supervision, J.G.F., J.-S.L. and W.J.; Visualization, K.A., J.G.F. and J.-S.L.; Writing—original draft, K.A. and J.-S.L.; Writing—review and editing, K.A., J.G.F. and J.-S.L. All authors have read and agreed to the published version of the manuscript.

Funding: This work was supported by a National Research Foundation of Korea (NRF) grant funded by the Korean government (MSIT) (No. 2021R1F1A1046778). Jong-Sook Lee was supported by a National Research Foundation of Korea (NRF) grant funded by the Ministry of Science and ICT (MSIT) (Grant No. NRF-2018R1A5A1025224).

Data Availability Statement: The original contributions presented in the study are included in the article; further inquiries can be directed to the corresponding author/s.

Acknowledgments: The authors would like to thank Nazım Ecebaş for assistance with the tape-casting studies. The authors would like to thank Kyeong-Kap Jeong and Jung-Yeol Park (Centre for Research Facilities, Chonnam National University) for operating the XRD and EPMA, respectively, and Hey-Jeong Kim (Centre for Development of Fine Chemicals, Chonnam National University) for operating the SEM.

Conflicts of Interest: The authors declare no conflicts of interest. The funders had no role in the design of the study; in the collection, analyses, or interpretation of data; in the writing of the manuscript; or in the decision to publish the results.

References

1. Rödel, J.; Jo, W.; Seifert, K.T.P.; Anton, E.M.; Granzow, T.; Damjanovic, D. Perspective on the Development of Lead-free Piezoceramics. *J. Am. Ceram. Soc.* **2009**, *92*, 1153–1177. [CrossRef]
2. Kurihara, K.; Kondo, M. High-strain piezoelectric ceramics and applications to actuators. *Ceram. Int.* **2008**, *34*, 695–699. [CrossRef]
3. Haertling, G.H. Ferroelectric Ceramics: History and Technology. In *Ferroelectricity: The Fundamentals Collection*; Gonzalo, J.A., Jiménez, B., Eds.; Wiley-VCH Verlag GmbH & Co. KGaA: Weinheim, Germany, 2005; pp. 157–178. [CrossRef]
4. Jo, W.; Dittmer, R.; Acosta, M.; Zang, J.; Groh, C.; Sapper, E.; Wang, K.; Rödel, J. Giant electric-field-induced strains in lead-free ceramics for actuator applications—Status and perspective. *J. Electroceram.* **2012**, *29*, 71–93. [CrossRef]
5. Gao, X.; Yang, J.; Wu, J.; Xin, X.; Li, Z.; Yuan, X.; Shen, X.; Dong, S. Piezoelectric Actuators and Motors: Materials, Designs, and Applications. *Adv. Mater. Technol.* **2020**, *5*, 1900716. [CrossRef]
6. Wu, J. *Advances in Lead-Free Piezoelectric Materials*; Springer Nature Singapore Pte Ltd.: Singapore, 2018.
7. Jones, G.O.; Thomas, P.A. Investigation of the structure and phase transitions in the novel A-site substituted distorted perovskite compound $Na_{0.5}Bi_{0.5}TiO_3$. *Acta Crystallogr. Sect. B* **2002**, *58*, 168–178. [CrossRef] [PubMed]
8. Aksel, E.; Forrester, J.S.; Jones, J.L.; Thomas, P.A.; Page, K.; Suchomel, M.R. Monoclinic crystal structure of polycrystalline $Na_{0.5}Bi_{0.5}TiO_3$. *Appl. Phys. Lett.* **2011**, *98*, 152901. [CrossRef]
9. Parija, B.; Badapanda, T.; Panigrahi, S.; Sinha, T.P. Ferroelectric and piezoelectric properties of $(1 - x)$ $(Bi_{0.5}Na_{0.5})TiO_3$–$xBaTiO_3$ ceramics. *J. Mater. Sci. Mater. Electron.* **2012**, *24*, 402–410. [CrossRef]
10. Zhang, Y.R.; Li, J.F.; Zhang, B.P. Enhancing Electrical Properties in NBT–KBT Lead-Free Piezoelectric Ceramics by Optimizing Sintering Temperature. *J. Am. Ceram. Soc.* **2008**, *91*, 2716–2719. [CrossRef]
11. Guo, Y.; Gu, M.; Luo, H.; Liu, Y.; Withers, R.L. Composition-induced antiferroelectric phase and giant strain in lead-free $(Na_y,Bi_z)Ti_{1-x}O_{3(1-x)}$-$xBaTiO_3$ ceramics. *Phys. Rev. B* **2011**, *83*, 054118. [CrossRef]
12. Hiruma, Y.; Nagata, H.; Takenaka, T. Thermal depoling process and piezoelectric properties of bismuth sodium titanate ceramics. *J. Appl. Phys.* **2009**, *105*, 084112. [CrossRef]
13. Hiruma, Y.; Imai, Y.; Watanabe, Y.; Nagata, H.; Takenaka, T. Large electrostrain near the phase transition temperature of $(Bi_{0.5}Na_{0.5})TiO_3$–$SrTiO_3$ ferroelectric ceramics. *Appl. Phys. Lett.* **2008**, *92*, 262904. [CrossRef]
14. Guo, Y.; Liu, Y.; Withers, R.L.; Brink, F.; Chen, H. Large Electric Field-Induced Strain and Antiferroelectric Behavior in $(1 - x)(Na_{0.5}Bi_{0.5})TiO_3$-$xBaTiO_3$ Ceramics. *Chem. Mater.* **2011**, *23*, 219–228. [CrossRef]
15. Teranishi, S.; Suzuki, M.; Noguchi, Y.; Miyayama, M.; Moriyoshi, C.; Kuroiwa, Y.; Tawa, K.; Mori, S. Giant strain in lead-free $(Bi_{0.5}Na_{0.5})TiO_3$-based single crystals. *Appl. Phys. Lett.* **2008**, *92*, 182905. [CrossRef]
16. Liu, X.; Tan, X. Giant Strains in Non-Textured $(Bi_{1/2}Na_{1/2})TiO_3$-Based Lead-Free Ceramics. *Adv. Mater.* **2016**, *28*, 574–578. [CrossRef]
17. Sheng, J.; Cao, W.P.; Li, W.L.; Lin, Q.R.; Li, M.L.; Hou, X.; Fei, W.D. Giant strain performance of lead-free relaxor piezoceramics through synergistic compositional and defect engineering. *Chem. Eng. J.* **2023**, *475*, 145989. [CrossRef]
18. Li, F.; Jin, L.; Xu, Z.; Zhang, S. Electrostrictive effect in ferroelectrics: An alternative approach to improve piezoelectricity. *Appl. Phys. Rev.* **2014**, *1*, 011103. [CrossRef]
19. Khan, N.U.; Yun, W.S.; Ullah, A.; Ali, S.; Sheeraz, M.; Ullah, A.; Kim, I.W.; Ahn, C.W. Large electrostrictive response via tailoring ergodic relaxor state in $Bi_{1/2}Na_{1/2}TiO_3$-based ceramics with $Bi(Mn_{1/2}Ce_{1/2})O_3$ end-member. *Ceram. Int.* **2024**, *50*, 8790–8799. [CrossRef]
20. Zhang, S.-T.; Kounga, A.B.; Jo, W.; Jamin, C.; Seifert, K.; Granzow, T.; Rödel, J.; Damjanovic, D. High-Strain Lead-free Antiferroelectric Electrostrictors. *Adv. Mater.* **2009**, *21*, 4716–4720. [CrossRef]
21. Ullah, A.; Gul, H.B.; Ullah, A.; Sheeraz, M.; Bae, J.-S.; Jo, W.; Ahn, C.W.; Kim, I.W.; Kim, T.H. Giant room-temperature electrostrictive coefficients in lead-free relaxor ferroelectric ceramics by compositional tuning. *APL Mater.* **2018**, *6*, 016104. [CrossRef]
22. Yao, K.; Zhou, C.; Li, Q.; Xiao, Z.; Yuan, C.; Xu, J.; Chen, G.; Rao, G. Large electrostrictive coefficient with optimized Electro-Strain in BNT-based ceramics with ergodic state. *Mater. Sci. Eng. B* **2022**, *283*, 115828. [CrossRef]
23. Jing, R.; Hu, Q.; Zhang, L.; Sun, Y.; Wu, J.; Alikin, D.O.; Shur, V.Y.; Wei, X.; Du, H.; Chang, Y.; et al. Ultra-slim electrostrains with superior temperature-stability in lead-free sodium niobate-based ferroelectric perovskite. *J. Mater.* **2022**, *8*, 1230–1238. [CrossRef]

24. Duraisamy, D.; Venkatesan, G.N. Compositionally driven giant strain and electrostrictive co-efficient in lead free NBT-BT-BFO system. *Appl. Phys. Lett.* **2018**, *112*, 052903. [CrossRef]
25. Swain, S.; Kumar Kar, S.; Kumar, P. Dielectric, optical, piezoelectric and ferroelectric studies of NBT–BT ceramics near MPB. *Ceram. Int.* **2015**, *41*, 10710–10717. [CrossRef]
26. Zhang, Q.; Zhao, X.; Sun, R.; Luo, H. Crystal growth and electric properties of lead-free NBT-BT at compositions near the morphotropic phase boundary. *Phys. Status Solidi (A)* **2011**, *208*, 1012–1020. [CrossRef]
27. Lv, J.; Li, Q.; Li, Y.; Tang, M.; Jin, D.; Yan, Y.; Fan, B.; Jin, L.; Liu, G. Significantly improved energy storage performance of NBT-BT based ceramics through domain control and preparation optimization. *Chem. Eng. J.* **2021**, *420*, 129900. [CrossRef]
28. Kanuru, S.R.; Baskar, K.; Dhanasekaran, R. Synthesis, structural, morphological and electrical properties of NBT–BT ceramics for piezoelectric applications. *Ceram. Int.* **2016**, *42*, 6054–6064. [CrossRef]
29. Liu, K.; Zhang, Y.; Marwat, M.A.; Wang, G.; Wang, D.; Ma, W.; Wei, T.; Li, M.; Xu, J.; Yang, H.; et al. Large electrostrain in low-temperature sintered NBT-BT-0.025FN incipient piezoceramics. *J. Am. Ceram. Soc.* **2020**, *103*, 3739–3747. [CrossRef]
30. Sapper, E.; Novak, N.; Jo, W.; Granzow, T.; Rödel, J. Electric-field–temperature phase diagram of the ferroelectric relaxor system $(1-x)Bi_{1/2}Na_{1/2}TiO_3 - xBaTiO_3$ doped with manganese. *J. Appl. Phys.* **2014**, *115*, 194104. [CrossRef]
31. Wang, F.; Xu, M.; Tang, Y.; Wang, T.; Shi, W.; Leung, C.M. Large Strain Response in the Ternary $Bi_{0.5}Na_{0.5}TiO_3$–$BaTiO_3$–$SrTiO_3$ Solid Solutions. *J. Am. Ceram. Soc.* **2012**, *95*, 1955–1959. [CrossRef]
32. Wang, F.; Jin, C.; Yao, Q.; Shi, W. Large electrostrictive effect in ternary $Bi_{0.5}Na_{0.5}TiO_3$-based solid solutions. *J. Appl. Phys.* **2013**, *114*, 027004. [CrossRef]
33. Zang, J.; Li, M.; Sinclair, D.C.; Jo, W.; Rödel, J. Impedance Spectroscopy of $(Bi_{1/2}Na_{1/2})TiO_3$–$BaTiO_3$ Ceramics Modified with $(K_{0.5}Na_{0.5})NbO_3$. *J. Am. Ceram. Soc.* **2014**, *97*, 1523–1529. [CrossRef]
34. Le, P.G.; Pham, T.L.; Nguyen, D.T.; Lee, J.S.; Fisher, J.G.; Kim, H.P.; Jo, W. Solid state crystal growth of single crystals of $0.75(Na_{1/2}Bi_{1/2})TiO_3$-$0.25SrTiO_3$ and their characteristic electrical properties. *J. Asian Ceram. Soc.* **2021**, *9*, 40–51. [CrossRef]
35. Bai, W.; Xi, J.; Zhang, J.; Shen, B.; Zhai, J.; Yan, H. Effect of different templates on structure evolution and large strain response under a low electric field in <001>-textured lead-free BNT-based piezoelectric ceramics. *J. Eur. Ceram. Soc.* **2015**, *35*, 2489–2499. [CrossRef]
36. Zhou, X.; Yang, H.; Xue, G.; Luo, H.; Zhang, D. Optimized strain performance in <001>-textured $Bi_{0.5}Na_{0.5}TiO_3$-based ceramics with ergodic relaxor state and core—Shell microstructure. *J. Adv. Ceram.* **2022**, *11*, 1542–1558. [CrossRef]
37. Hussain, A.; Maqbool, A.; Malik, R.A.; Ahmed, T.; Lee, S.; Kim, M.-H. Texture performance of lead-free $Bi_{1/2}Na_{1/2}TiO_3$–$BaZrO_3$ ceramics. *Ceram. Int.* **2023**, *49*, 10073–10082. [CrossRef]
38. Gao, F.; Hong, R.-Z.; Liu, J.-J.; Yao, Y.-H.; Tian, C.-S. Effect of different templates on microstructure of textured $Na_{0.5}Bi_{0.5}TiO_3$–$BaTiO_3$ ceramics with RTGG method. *J. Eur. Ceram. Soc.* **2008**, *28*, 2063–2070. [CrossRef]
39. Jiang, C.; Zhou, X.; Zhou, K.; Chen, C.; Luo, H.; Yuan, X.; Zhang, D. Grain oriented $Na_{0.5}Bi_{0.5}TiO_3$-$BaTiO_3$ ceramics with giant strain response derived from single-crystalline $Na_{0.5}Bi_{0.5}TiO_3$-$BaTiO_3$ templates. *J. Eur. Ceram. Soc.* **2016**, *36*, 1377–1383. [CrossRef]
40. Liu, K.; Ma, W.; Ben, N.; Zhu, H.; Xu, W.; Gao, H.; Samart, C.; Kongparakul, S.; Zhang, H.; Tan, H. Superior Large-Signal Piezoelectric Coefficient in Textured NBT-Based Piezoceramics by Template-Induced Structure and Composition Modulation. *ACS Appl. Mater. Interfaces* **2023**, *15*, 24595–24605. [CrossRef]
41. Bai, W.; Chen, D.; Zheng, P.; Xi, J.; Zhou, Y.; Shen, B.; Zhai, J.; Ji, Z. $NaNbO_3$ templates-induced phase evolution and enhancement of electromechanical properties in <00l> grain oriented lead-free BNT-based piezoelectric materials. *J. Eur. Ceram. Soc.* **2017**, *37*, 2591–2604. [CrossRef]
42. Ahn, C.W.; Choi, G.; Kim, I.W.; Lee, J.S.; Wang, K.; Hwang, Y.; Jo, W. Forced electrostriction by constraining polarization switching enhances the electromechanical strain properties of incipient piezoceramics. *NPG Asia Mater.* **2017**, *9*, e346. [CrossRef]
43. Chang, Y.; Yang, Z.; Chao, X.; Liu, Z.; Wang, Z. Synthesis and morphology of anisotropic $NaNbO_3$ seed crystals. *Mater. Chem. Phys.* **2008**, *111*, 195–200. [CrossRef]
44. Zhang, M.; Fan, H.; Chen, L.; Yang, C. Synthesis and formation mechanisms of high aspect ratio platelike $NaNbO_3$ particles by topochemical microcrystal conversion. *J. Alloys Compd.* **2009**, *476*, 847–853. [CrossRef]
45. Mathur, L.; Bae, H.; Namgung, Y.; Park, J.-Y.; Song, S.-J. Flow behavior of gadolinium doped ceria under different polymeric and hydrodynamic environment for tape casting application. *Korean J. Chem. Eng.* **2022**, *39*, 2991–3002. [CrossRef]
46. Lotgering, F.K. Topotactical reactions with ferrimagnetic oxides having hexagonal crystal structures—I. *J. Inorg. Nucl. Chem.* **1959**, *9*, 113–123. [CrossRef]
47. Moriana, A.D.; Zhang, S. Lead-free textured piezoceramics using tape casting: A review. *J. Mater.* **2018**, *4*, 277–303. [CrossRef]
48. Park, S.-E.; Shrout, T.R. Ultrahigh strain and piezoelectric behavior in relaxor based ferroelectric single crystals. *J. Appl. Phys.* **1997**, *82*, 1804–1811. [CrossRef]
49. Chen, C.; Wang, Y.; Jiang, X.; Tu, N.; Chen, Y.; Zhou, S.; Xia, X.; Shen, Z.; Luo, H. Orientation dependence of electric field induced phase transitions in lead-free $(Na_{0.5}Bi_{0.5})TiO_3$-based single crystals. *J. Am. Ceram. Soc.* **2019**, *102*, 4306–4313. [CrossRef]
50. Ge, W.; Liu, H.; Zhao, X.; Li, X.; Pan, X.; Lin, D.; Xu, H.; Jiang, X.; Luo, H. Orientation dependence of electrical properties of $0.96Na_{0.5}Bi_{0.5}TiO_3$-$0.04BaTiO_3$ lead-free piezoelectric single crystal. *Appl. Phys. A* **2009**, *95*, 761–767. [CrossRef]

51. Yu, H.-L.; Ko, N.-R.; Choi, W.-J.; Zate, T.T.; Jo, W. A Brief Review of Some Challenging Issues in Textured Piezoceramics via Templated Grain Growth Method. *J. Sens. Sci. Technol.* **2023**, *32*, 10–15. [CrossRef]
52. Zhao, W.; Ya, J.; Xin, Y.; E, L.; Zhao, D.; Zhou, H. Fabrication of $Na_{0.5}Bi_{0.5}TiO_3$–$BaTiO_3$-Textured Ceramics Templated by Plate-Like $Na_{0.5}Bi_{0.5}TiO_3$ Particles. *J. Am. Ceram. Soc.* **2009**, *92*, 1607–1609. [CrossRef]
53. Bai, W.; Chen, D.; Zheng, P.; Zhang, J.; Shen, B.; Zhai, J.; Ji, Z. Grain-orientated lead-free BNT-based piezoceramics with giant electrostrictive effect. *Ceram. Int.* **2017**, *43*, 3339–3345. [CrossRef]
54. Zeng, J.T.; Kwok, K.W.; Tam, W.K.; Tian, H.Y.; Jiang, X.P.; Chan, H.L.W. Plate-Like $Na_{0.5}Bi_{0.5}TiO_3$ Template Synthesized by a Topochemical Method. *J. Am. Ceram. Soc.* **2006**, *89*, 3850–3853. [CrossRef]
55. Kimura, T.; Takahashi, T.; Tani, T.; Saito, Y. Preparation of crystallographically textured $Bi_{0.5}Na_{0.5}TiO_3$–$BaTiO_3$ ceramics by reactive-templated grain growth method. *Ceram. Int.* **2004**, *30*, 1161–1167. [CrossRef]
56. Kong, S.; Kumar, N.; Checchia, S.; Cazorla, C.; Daniels, J. Defect-Driven Structural Distortions at the Surface of Relaxor Ferroelectrics. *Adv. Funct. Mater.* **2019**, *29*, 1900344. [CrossRef]
57. Kumar, N.; Kong, S.; Sharma, P.; Shi, X.; Vats, G.; Checchia, S.; Seidel, J.; Hoffman, M.; Daniels, J. Functional surface layers in relaxor ferroelectrics. *J. Mater. Chem. C* **2020**, *8*, 7663–7671. [CrossRef]
58. Zhang, D.; Zhang, S.; Yuan, X.; Zhou, X.; Qi, H.; Yan, M.; Yan, Z.; Zhou, K. Enhanced piezoelectric properties in textured $NaNbO_3$–$BaTiO_3$–$SrZrO_3$ ceramics by templated grain growth. *J. Alloys Compd.* **2020**, *843*, 155865. [CrossRef]
59. Chang, Y.; Sun, Y.; Wu, J.; Wang, X.; Zhang, S.; Yang, B.; Messing, G.L.; Cao, W. Formation mechanism of highly [001]c textured $Pb(In_{1/2}Nb_{1/2})O_3$-$Pb(Mg_{1/3}Nb_{2/3})O_3$-$PbTiO_3$ relaxor ferroelectric ceramics with giant piezoelectricity. *J. Eur. Ceram. Soc.* **2016**, *36*, 1973–1981. [CrossRef]
60. Maurya, D.; Zhou, Y.; Yan, Y.; Priya, S. Synthesis mechanism of grain-oriented lead-free piezoelectric $Na_{0.5}Bi_{0.5}TiO_3$-$BaTiO_3$ ceramics with giant piezoelectric response. *J. Mater. Chem. C* **2013**, *1*, 2102–2111. [CrossRef]
61. Salimkhani, H.; Fulanović, L.; Frömling, T. Sinterability of sodium bismuth titanate-based electroceramics at low temperatures. *J. Eur. Ceram. Soc.* **2024**, *44*, 1570–1580. [CrossRef]
62. Sung, Y.S.; Kim, J.M.; Cho, J.H.; Song, T.K.; Kim, M.H.; Chong, H.H.; Park, T.G.; Do, D.; Kim, S.S. Effects of Na nonstoichiometry in $(Bi_{0.5}Na_{0.5+x})TiO_3$ ceramics. *Appl. Phys. Lett.* **2010**, *96*, 022901. [CrossRef]
63. Gadelmawla, A.; Riess, K.; Birkenstock, J.; Hinterstein, M.; Webber, K.G.; Khansur, N.H. Effect of varying Bi content on the temperature-dependent mechanical, dielectric, and structural properties of nominal $Na_{1/2}Bi_{1/2}TiO_3$. *J. Appl. Phys.* **2021**, *130*, 185106. [CrossRef]
64. Zhang, A.; Jing, R.; Zhuang, M.; Hou, H.; Zhang, L.; Zhang, J.; Lu, X.; Yan, Y.; Du, H.; Jin, L. Nonstoichiometric effect of A-site complex ions on structural, dielectric, ferroelectric, and electrostrain properties of bismuth sodium titanate ceramics. *Ceram. Int.* **2021**, *47*, 32747–32755. [CrossRef]
65. Li, L.; Li, M.; Zhang, H.; Reaney, I.M.; Sinclair, D.C. Controlling mixed conductivity in $Na_{1/2}Bi_{1/2}TiO_3$ using A-site non-stoichiometry and Nb-donor doping. *J. Mater. Chem. C* **2016**, *4*, 5779–5786. [CrossRef]
66. Han, J.; Yin, J.; Wu, J. BNT-based ferroelectric ceramics: Electrical properties modification by Ta_2O_5 oxide addition. *J. Am. Ceram. Soc.* **2020**, *103*, 412–422. [CrossRef]
67. Craciun, F.; Galassi, C.; Birjega, R. Electric-field-induced and spontaneous relaxor-ferroelectric phase transitions in $(Na_{1/2}Bi_{1/2})_{1-x}BaxTiO_3$. *J. Appl. Phys.* **2012**, *112*, 124106. [CrossRef]
68. Jin, L.; Li, F.; Zhang, S. Decoding the Fingerprint of Ferroelectric Loops: Comprehension of the Material Properties and Structures. *J. Am. Ceram. Soc.* **2014**, *97*, 1–27. [CrossRef]
69. Liu, G.; Dong, J.; Zhang, L.; Yan, Y.; Jing, R.; Jin, L. Phase evolution in $(1-x)(Na_{0.5}Bi_{0.5})TiO_3$-$xSrTiO_3$ solid solutions: A study focusing on dielectric and ferroelectric characteristics. *J. Mater.* **2020**, *6*, 677–691. [CrossRef]
70. Liu, X.; Shen, B.; Zhai, J. Designing novel sodium bismuth titanate lead-free incipient perovskite for piezoactuator applications. *J. Am. Ceram. Soc.* **2019**, *102*, 6751–6759. [CrossRef]
71. Dittmer, R.; Gobeljic, D.; Jo, W.; Shvartsman, V.V.; Lupascu, D.C.; Jones, J.L.; Rödel, J. Ergodicity reflected in macroscopic and microscopic field-dependent behavior of BNT-based relaxors. *J. Appl. Phys.* **2014**, *115*, 084111. [CrossRef]
72. Le, P.G.; Tran, T.L.; Kim, H.P.; Jo, W.; Lee, J.S.; Fisher, J.G. Growth of single crystals of $0.75(Na_{0.5}Bi_{0.5})TiO_3$-$0.25(Sr_{0.7}Ca_{0.3})TiO_3$ and characterisation of their electrical properties. *Open Ceram.* **2021**, *6*, 100099. [CrossRef]
73. Bai, W.; Li, L.; Wang, W.; Shen, B.; Zhai, J. Phase diagram and electrostrictive effect in BNT-based ceramics. *Solid State Commun.* **2015**, *206*, 22–25. [CrossRef]
74. Shi, J.; Fan, H.; Liu, X.; Bell, A.J. Large Electrostrictive Strain in $(Bi_{0.5}Na_{0.5})TiO_3$–$BaTiO_3$–$(Sr_{0.7}Bi_{0.2})TiO_3$ Solid Solutions. *J. Am. Ceram. Soc.* **2014**, *97*, 848–853. [CrossRef]
75. Wu, J.; Zhang, H.; Huang, C.-H.; Tseng, C.-W.; Meng, N.; Koval, V.; Chou, Y.-C.; Zhang, Z.; Yan, H. Ultrahigh field-induced strain in lead-free ceramics. *Nano Energy* **2020**, *76*, 105037. [CrossRef]
76. Singha, A.; Praharaj, S.; Rout, S.K.; Rout, D. Composition dependent crossover from ferroelectric to relaxor-ferroelectric in NBT-ST-KNN ceramics. *Curr. Appl. Phys.* **2022**, *36*, 160–170. [CrossRef]
77. Ullah, A.; Malik, R.A.; Ullah, A.; Lee, D.S.; Jeong, S.J.; Lee, J.S.; Kim, I.W.; Ahn, C.W. Electric-field-induced phase transition and large strain in lead-free Nb-doped BNKT-BST ceramics. *J. Eur. Ceram. Soc.* **2014**, *34*, 29–35. [CrossRef]

78. Deng, A.; Wu, J. Optimized strain properties with small hysteresis in BNT-based ceramics with ergodic relaxor state. *J. Eur. Ceram. Soc.* **2021**, *41*, 5147–5154. [CrossRef]
79. Bai, W.; Wang, L.; Zheng, P.; Wen, F.; Yuan, Y.; Ding, M.; Chen, D.; Zhai, J.; Ji, Z. Large electrostrictive effect in lead-free $(Bi_{.5}Na_{.5})TiO_3$-based composite piezoceramics. *Ceram. Int.* **2018**, *44*, 8628–8634. [CrossRef]
80. Hao, J.; Xu, Z.; Chu, R.; Li, W.; Fu, P.; Du, J.; Li, G. Large electrostrictive effect and strong photoluminescence in rare-earth modified lead-free $(Bi_{0.5}Na_{0.5})TiO_3$-based piezoelectric ceramics. *Scr. Mater.* **2016**, *122*, 10–13. [CrossRef]
81. Ang, C.; Yu, Z. High, Purely Electrostrictive Strain in Lead-Free Dielectrics. *Adv. Mater.* **2006**, *18*, 103–106. [CrossRef]
82. Li, F.; Jin, L.; Guo, R. High electrostrictive coefficient Q_{33} in lead-free $Ba(Zr_{0.2}Ti_{0.8})O_3$-x$(Ba_{0.7}Ca_{0.3})TiO_3$ piezoelectric ceramics. *Appl. Phys. Lett.* **2014**, *105*, 232903. [CrossRef]
83. Li, F.; Jin, L.; Xu, Z.; Wang, D.; Zhang, S. Electrostrictive effect in $Pb(Mg_{1/3}Nb_{2/3})O_3$-x$PbTiO_3$ crystals. *Appl. Phys. Lett.* **2013**, *102*, 152910. [CrossRef]
84. Hao, J.; Xu, Z.; Chu, R.; Li, W.; Fu, P.; Du, J.; Li, G. Structure evolution and electrostrictive properties in (Bi0.5Na0.5)0.94Ba0.06TiO3–M2O5 (M=Nb, Ta, Sb) lead-free piezoceramics. *J. Eur. Ceram. Soc.* **2016**, *36*, 4003–4014. [CrossRef]
85. Tran, V.D.N.; Dinh, T.H.; Han, H.-S.; Jo, W.; Lee, J.-S. Lead-free $Bi_{1/2}(Na_{0.82}K_{0.18})_{1/2}TiO_3$ relaxor ferroelectrics with temperature insensitive electrostrictive coefficient. *Ceram. Int.* **2013**, *39*, S119–S124. [CrossRef]
86. Yang, S.; Li, J.; Liu, Y.; Wang, M.; Qiao, L.; Gao, X.; Chang, Y.; Du, H.; Xu, Z.; Zhang, S.; et al. Textured ferroelectric ceramics with high electromechanical coupling factors over a broad temperature range. *Nat. Commun.* **2021**, *12*, 1414. [CrossRef]
87. Qi, H.; Zuo, R. Giant electrostrictive strain in $(Bi_{0.5}Na_{0.5})TiO_3$–$NaNbO_3$ lead-free relaxor antiferroelectrics featuring temperature and frequency stability. *J. Mater. Chem. A* **2020**, *8*, 2369–2375. [CrossRef]
88. Li, F.; Xu, Z.; Zhang, S. The effect of polar nanoregions on electromechanical properties of relaxor-$PbTiO_3$ crystals: Extracting from electric-field-induced polarization and strain behaviors. *Appl. Phys. Lett.* **2014**, *105*, 122904. [CrossRef]
89. Cao, W.P.; Sheng, J.; Qiao, Y.L.; Jing, L.; Liu, Z.; Wang, J.; Li, W.L. Optimized strain with small hysteresis and high energy-storage density in Mn-doped NBT-ST system. *J. Eur. Ceram. Soc.* **2019**, *39*, 4046–4052. [CrossRef]
90. Cao, W.; Li, W.; Feng, Y.; Bai, T.; Qiao, Y.; Hou, Y.; Zhang, T.; Yu, Y.; Fei, W. Defect dipole induced large recoverable strain and high energy-storage density in lead-free $Na_{0.5}Bi_{0.5}TiO_3$-based systems. *Appl. Phys. Lett.* **2016**, *108*, 202902. [CrossRef]
91. Zhang, S.-T.; Yan, F.; Yang, B.; Cao, W. Phase diagram and electrostrictive properties of $Bi_{0.5}Na_{0.5}TiO_3$–$BaTiO_3$–$K_{0.5}Na_{0.5}NbO_3$ ceramics. *Appl. Phys. Lett.* **2010**, *97*, 122901. [CrossRef]
92. Hao, J.; Xu, Z.; Chu, R.; Li, W.; Du, J. Lead-free electrostrictive $(Bi_{0.5}Na_{0.5})TiO_3$–$(Bi_{0.5}K_{0.5})TiO_3$–$(K_{0.5}Na_{0.5})NbO_3$ ceramics with good thermostability and fatigue-free behavior. *J. Mater. Sci.* **2015**, *50*, 5328–5336. [CrossRef]
93. Liu, X.; Xue, S.; Ma, J.; Zhai, J.; Shen, B.; Wang, F.; Zhao, X.; Yan, H. Electric-field-induced local distortion and large electrostrictive effects in lead-free NBT-based relaxor ferroelectrics. *J. Eur. Ceram. Soc.* **2018**, *38*, 4631–4639. [CrossRef]
94. Tang, X.; Liu, L.; Guo, L.; Li, L.; Guo, Y.; Guan, Q.; Ren, M.; Hao, J.; Li, W. High-temperature and long-term stability in Co/Sb-codoped $(Bi_{0.5}Na_{0.5})TiO_3$-based electrostrictive ceramics. *J. Alloys Compd.* **2021**, *876*, 160202. [CrossRef]
95. Liu, X.; Zhao, Y.; Shi, J.; Du, H.; Xu, X.; Lu, H.; Che, J.; Li, X. Improvement of dielectric and ferroelectric properties in bismuth sodium titanate based relaxors through Bi non-stoichiometry. *J. Alloys Compd.* **2019**, *799*, 231–238. [CrossRef]
96. Praharaj, S.; Rout, D.; Kang, S.J.L.; Kim, I.W. Large electric field induced strain in a new lead-free ternary $Na_{0.5}Bi_{0.5}TiO_3$-$SrTiO_3$-$BaTiO_3$ solid solution. *Mater. Lett.* **2016**, *184*, 197–199. [CrossRef]
97. Zhang, H.; Xu, P.; Patterson, E.; Zang, J.; Jiang, S.; Rödel, J. Preparation and enhanced electrical properties of grain-oriented (Bi1/2Na1/2)TiO3-based lead-free incipient piezoceramics. *J. Eur. Ceram. Soc.* **2015**, *35*, 2501–2512. [CrossRef]
98. Sung, Y.S.; Kim, J.M.; Cho, J.H.; Song, T.K.; Kim, M.H.; Park, T.G. Effects of Bi nonstoichiometry in $(Bi_{0.5+x}Na)$ TiO_3 ceramics. *Appl. Phys. Lett.* **2011**, *98*, 012902. [CrossRef]
99. Mishra, A.; Khatua, D.K.; De, A.; Majumdar, B.; Frömling, T.; Ranjan, R. Structural mechanism behind piezoelectric enhancement in off-stoichiometric $Na_{0.5}Bi_{0.5}TiO_3$ based lead-free piezoceramics. *Acta Mater.* **2019**, *164*, 761–775. [CrossRef]
100. Shvartsman, V.V.; Lupascu, D.C. Lead-Free Relaxor Ferroelectrics. *J. Am. Ceram. Soc.* **2012**, *95*, 1–26. [CrossRef]
101. Jo, W.; Schaab, S.; Sapper, E.; Schmitt, L.A.; Kleebe, H.J.; Bell, A.J.; Rödel, J. On the phase identity and its thermal evolution of lead free $(Bi_{1/2}Na_{1/2})TiO_3$-6 mol% $BaTiO_3$. *J. Appl. Phys.* **2011**, *110*, 074106. [CrossRef]
102. Fisher, J.G.; Sim, S.-H.; Đoàn, T.T.; Uwiragiye, E.; Mok, J.; Lee, J. Comparison of $(K_{0.5}Na_{0.5})NbO_3$ Single Crystals Grown by Seed-Free and Seeded Solid-State Single Crystal Growth. *Materials* **2023**, *16*, 3638. [CrossRef] [PubMed]
103. Uwiragiye, E.; Pham, T.L.; Lee, J.-S.; Lee, B.-W.; Ko, J.-H.; Fisher, J.G. $0.98(K_{0.5}Na_{0.5})NbO_3$–$0.02(Bi_{0.5}Na_{0.5})(Zr_{0.85}Sn_{0.15})O_3$ Single Crystals Grown by the Seed-Free Solid-State Crystal Growth Method and Their Characterization. *Ceramics* **2024**, *7*, 840–857. [CrossRef]
104. Fridkin, V.M. Thermodynamics of Ferroelectric Semiconductors. In *Ferroelectric Semiconductors*; Consultants Bureau: New York, NY, USA, 1980; Chapter 1; pp. 1–21.
105. Landau, L.D.; Lifshitz, E.M. Chapter XIV—Phase Transitions of the Second Kind and Critical Phenomena. In *Statistical Physics*, 3rd ed.; Landau, L.D., Lifshitz, E.M., Eds.; Butterworth-Heinemann: Pergamon, Turkey, 1980; Volume 5, pp. 446–516.
106. Fisher, J.G.; Park, H.Y.; Song, Y.O.; Baek, S.J.; Vu, H.; Kim, J.H.; Kim, Y.H.; Lee, J.S. Sintering, microstructure and electrical properties of $0.4(Bi_{0.5}K_{0.5})TiO_3$-$0.6BiFeO_3$ lead-free piezoelectric ceramics. *J. Korean Phys. Soc.* **2016**, *68*, 59–67. [CrossRef]
107. Anton, E.-M.; Jo, W.; Damjanovic, D.; Rödel, J. Determination of depolarization temperature of $(Bi_{1/2}Na_{1/2})TiO_3$-based lead-free piezoceramics. *J. Appl. Phys.* **2011**, *110*, 094108. [CrossRef]

108. Trung, D.T.; Uwiragiye, E.; Lan, T.T.; Fisher, J.G.; Lee, J.-S.; Mok, J.; Lee, J.; Naqvi, F.U.H.; Ko, J.-H. Growth of Single Crystals of $(K_{1-x}Na_x)NbO_3$ by the Self-Flux Method and Characterization of Their Phase Transitions. *Materials* **2024**, *17*, 4195. [CrossRef]
109. Abbas, A.; Jung, W.G.; Moon, W.J.; Uwiragiye, E.; Pham, T.L.; Lee, J.S.; Fisher, J.G.; Ge, W.; Naqvi, F.U.H.; Ko, J.H. Growth of $(1 - x)(Na_{1/2}Bi_{1/2})TiO_3$–$xKNbO_3$ single crystals by the self-flux method and their characterisation. *J. Korean Ceram. Soc.* **2024**, *61*, 342–365. [CrossRef]